

www.acsnano.org

Sulfur-Rich Graphene Nanoboxes with Ultra-High Potassiation Capacity at Fast Charge: Storage Mechanisms and Device Performance

Yiwei Sun, Huanlei Wang,* Wenrui Wei, Yulong Zheng, Lin Tao, Yixian Wang, Minghua Huang, Jing Shi, Zhi-Cheng Shi, and David Mitlin*



Downloaded via UNIV OF TEXAS AT AUSTIN on September 17, 2021 at 19:44:42 (UTC). See https://pubs.acs.org/sharingguidelines for options on how to legitimately share published articles.

Cite This: ACS Nano 2021, 15, 1652-1665



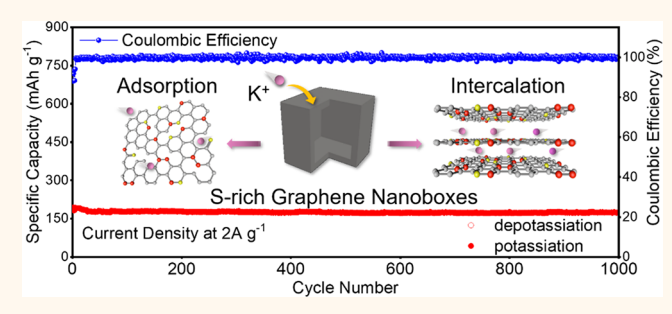
ACCESS I

Metrics & More

Article Recommendations

Supporting Information

ABSTRACT: It is a major challenge to achieve fast charging and high reversible capacity in potassium ion storing carbons. Here, we synthesized sulfur-rich graphene nanoboxes (SGNs) by one-step chemical vapor deposition to deliver exceptional rate and cyclability performance as potassium ion battery and potassium ion capacitor (PIC) anodes. The SGN electrode exhibits a record reversible capacity of 516 mAh g⁻¹ at 0.05 A g⁻¹, record fast charge capacity of 223 mA h g⁻¹ at 1 A g⁻¹, and exceptional stability with 89% capacity retention after 1000 cycles. Additionally, the SGN-based PIC displays highly favorable Ragone chart characteristics: 112 Wh kg⁻¹at 505 W



kg⁻¹ and 28 Wh kg⁻¹ at 14618 W kg⁻¹ with 92% capacity retention after 6000 cycles. X-ray photoelectron spectroscopy analysis illustrates a charge storage sequence based primarily on reversible ion binding at the structural-chemical defects in the carbon and the reversible formation of K-S-C and K₂S compounds. Transmission electron microscopy analysis demonstrates reversible dilation of graphene due to ion intercalation, which is a secondary source of capacity at low voltage. This intercalation mechanism is shown to be stable even at cycle 1000. Galvanostatic intermittent titration technique analysis yields diffusion coefficients from 10^{-10} to 10^{-12} cm² s⁻¹, an order of magnitude higher than S-free carbons. The direct electroanalytic/analytic comparison indicates that chemically bound sulfur increases the number of reversible ion bonding sites, promotes reaction-controlled over diffusion-controlled kinetics, and stabilizes the solid electrolyte interphase. It is also demonstrated that the initial Coulombic efficiency can be significantly improved by switching from a standard carbonate-based electrolyte to an ether-based one.

KEYWORDS: sulfur-doping, graphene, potassium sulfur battery, potassium metal battery, hybrid ion capacitor

otassium ion batteries (PIBs) and potassium ion capacitors (PICs) are drawing considerable scientific attention. 1-11 Potassium has a lower redox voltage than Li and Na (-0.09 V vs 0 and 0.23 V), implying that a relatively high voltage for a full battery may be possible. 12-15 Moreover, potassium has a weaker Lewis acidity than Li and Na, resulting in a smaller Stokes' radius (3.6 Å vs 4.8 and 4.6 Å) in carbonate solvents. 16,17 In a carbonate electrolyte, K+ obtains the highest ion mobility, ion conductivity, and ion transport number of the three ions. 18 A range of materials have been employed as PIB anodes, including MXene, phosphorus-based materials, V₂O₃based systems, potassium titanate, various metal alloys, and carbons. 19-28 For example, MXene-based anodes have demonstrated long-term cycling stability and adjustable layer spacing.¹⁹ Li et al. reported Sn₄P₃@C composite displaying 473 mAh g^{-1} at 50 mA g^{-1} and 182 mAh g^{-1} after 800 cycles at $0.5 \text{ A g}^{-1.29}$ When the cost, chemical stability, and environ-

mental sustainability are considered, carbonaceous materials have been regarded among the most promising PIB anode candidates.6,30-37

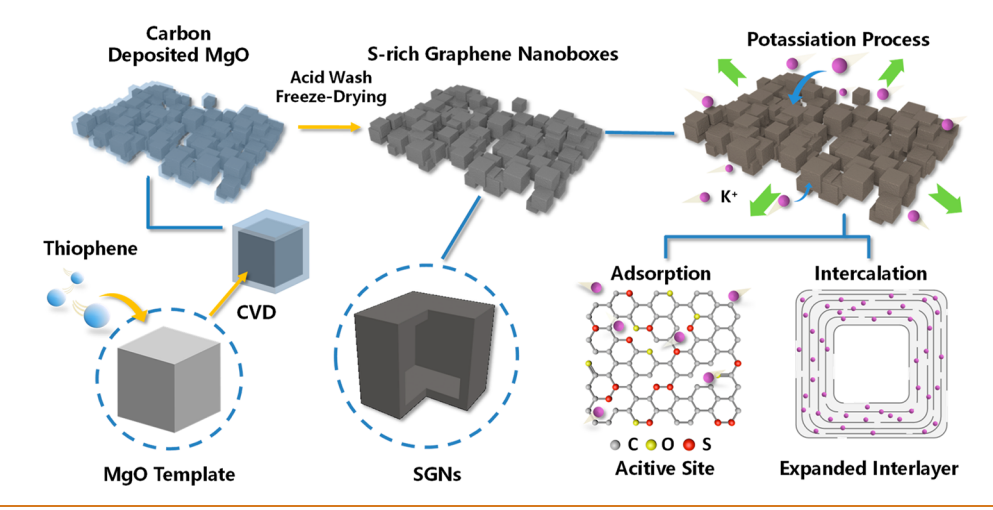
Analogously to lithium and distinct from sodium, potassium will reversibly intercalate into graphite, forming a graphitic intercalation compound (GIC).³⁸ The K-GIC delivers a reversible capacity of KC₈ (279 mAh g⁻¹) albeit at low charging rates.³⁹ Owing to the large radius of K⁺ (1.36 Å vs 0.76 Å for Li⁺) and associated severe strain (61% KC₈ vs 10%

Received: November 6, 2020 Accepted: December 21, 2020 Published: December 28, 2020





Scheme 1. Schematic Illustration for the Synthesis Processes, the Resulting Structure, and the Charge Storage Mechanisms for SGNs



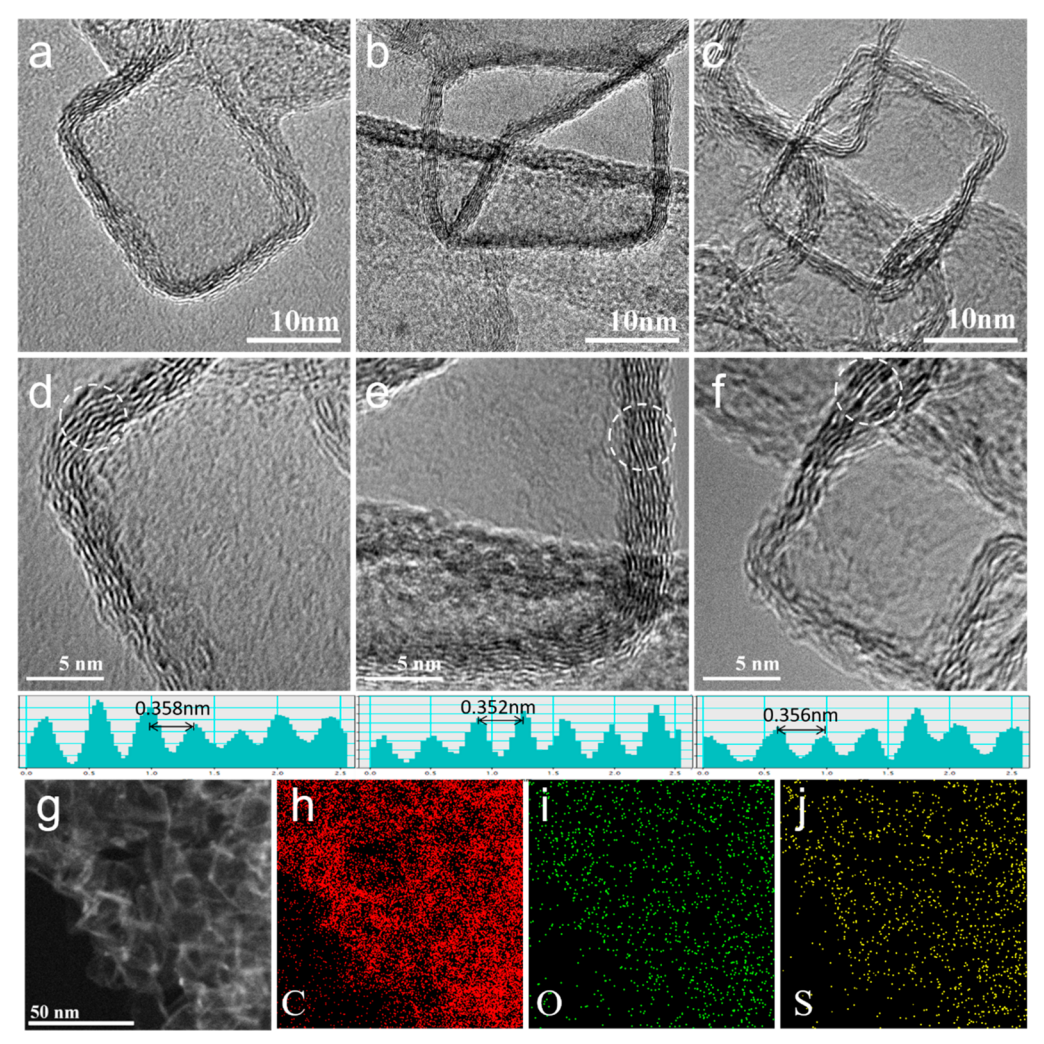


Figure 1. HRTEM images and corresponding graphene layer spacing profiles of (a, d) SGN-900, (b, e) SGN-1000, and (c, f) GN-900, respectively. (g-j) HAADF-STEM image and the corresponding EDXS elemental maps of C, O, and S for SGN-900.

 ${\rm LiC_6}$), graphite with K displays a relatively poor rate performance and cycling stability. Ji and co-workers reported a reversible potassiation process in graphite using a 0.8 M KPF₆ electrolyte in ethylene carbonate (EC)—diethyl carbonate (DEC). The galvanostatic curves display potassiation

and depotassiation plateaus, exhibiting capacities of 475 and 273 mAh $\rm g^{-1}$ at potassiation and depotassiation, respectively. The lowered intensity of the broadened X-ray diffraction (XRD) peaks of graphite after depotassiation indicated structural damage to graphite caused by the potassium

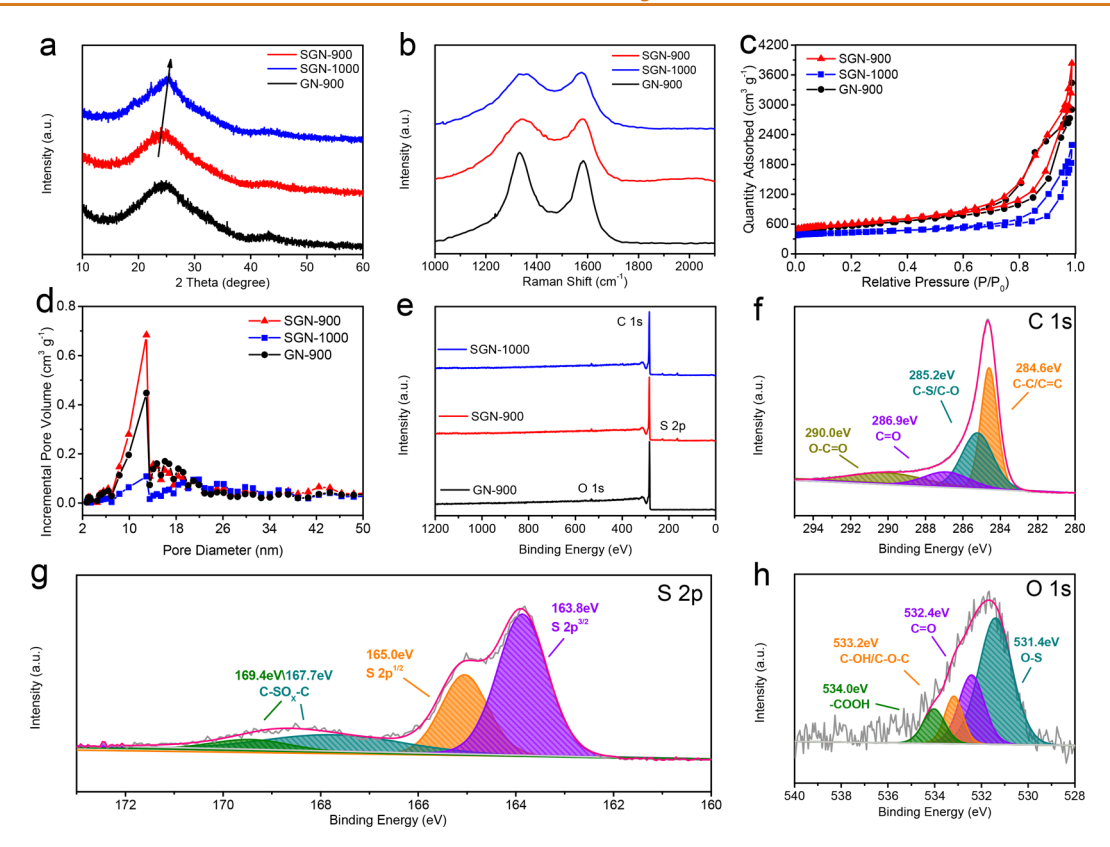


Figure 2. Structural, textural, and near-surface chemistry characterization of SGN-900, SGN-1000, and GN-900. (a) XRD patterns, (b) Raman spectra, (c) nitrogen adsorption—desorption isotherm curves, and (d) the corresponding pore size distributions. (e) The XPS survey spectra of SGNs and GN. High-resolution XPS spectra of SGN-900 and their corresponding fitting curves of (f) C 1s, (g) S 2p, and (h) O 1s.

insertion. To reveal the potassium storage mechanism in graphite, Raman and density functional theory calculation were employed. ^{38,42,43} The thermodynamically achievable potassiation of graphitic carbons was confirmed to be KC₈, giving a ceiling to the achievable capacity even in the most optimized architectures.

Methods such as electrolyte modification, optimized binder, expanded layer spacing, heteroatom doping, electrode architecture design, etc. have been employed to improve the electrochemical performance of carbons. 38,42-49 Employing hollow nanostructures in place of dense micro- or nanoelectrodes is an effective strategy to buffer the volume expansion during the potassiation/depotassiation process as well as to enhance the rate performance due to shorter diffusion distances.⁵⁰ For example, Song's group fabricated graphitic carbon nanocage electrodes with an interconnected structure, leading to excellent rate capability with a reversible capacity of 175 mAh g^{-1} at 9.8 A $g^{-1.51}$ Alshareef's group reported the nitrogen-doped graphitic nanocarbon electrode, showing a high capacity of 280 mAh g⁻¹ at 0.05 A g⁻¹ and a stabilized cycle life over 200 cycles. The introduction of heteroatoms into the carbon skeleton has proven to be a promising approach for promoting reversible capacity. 9,53,54 The defective structure and the expanded graphitic layer due to the heteroatoms promote both higher capacity and extended rate capability. 34,55,56 Nitrogen- and/or oxygen-doped carbon materials have been reported to enhance potassium storage through these means. 34,57,58 Guo and his group reported freestanding N-doped hollow carbon material through electrospinning as a high performance anode in PIBs. 57

While there are some emerging studies on S-doped carbons for potassium ion storage, overall, these are far fewer in number than for O- and N-doped carbons. For example, Mai's group reported sulfur-doped reduced graphene oxide sponges as anodes for PIBs, achieving a high specific capacity of 361 mAh g^{-1} at 0.5 A g^{-1} . Ding et al. synthesized and tested sulfur-doped hollow carbon spheres as anodes for PIBs. 12 Xie's group prepared phenolic resin derived hard carbon using sulfur powder for vulcanization as anodes for PIBs, exhibiting a capacity of 270 mA h g⁻¹ at 0.2 A g⁻¹ and excellent rate capability with 100 mA h g⁻¹ at 5 A g⁻¹.⁶⁰ For S-doped carbons with potassium ions, more "electrode architecture" and fundamental insight studies are warranted. Moreover, for PIB carbon-based anodes, it is challenging to achieve a combination of high capacity, fast charge capability, and long cycling life. Here, we synthesize S-rich carbons that simultaneously achieve these three objectives, displaying state-of-the-art electrochemical performance. In parallel, electroanalytical methods, advanced transmission electron microscopy (TEM), and surface science analysis are employed to provide insight on the charge storage mechanisms.

RESULTS AND DISCUSSION

Physicochemical Characterization of Sulfur-Rich Graphene Nanoboxes (SGNs). Scheme 1 illustrates the synthesis processes and charge storage mechanism for SGNs. Details of the synthesis procedure are provided in the Methods, while the charge storage mechanisms will be discussed throughout the text. To summarize the synthesis method, thiophene was employed as the sulfur-rich precursor and MgO was employed as a sacrificial template. Magnesium

carbonate hydroxide pentahydrate was heated in a nitrogen atmosphere to form MgO, after which point the thiophene vapor was introduced into the chamber. After cooling to room temperature, the MgO template was removed by chemical etching. The resulting material is denoted as SGN-900 and SGN-1000, representing a thiophene deposition temperature of 900 or 1000 °C. As a baseline, sulfur-free graphene nanoboxes were synthesized using ethanol as the precursor at 900 °C, termed GN-900.

Per the low magnification scanning electron microscopy (SEM) images in Figure S1, the SGN materials exhibit an interconnected flake-like morphology. Figure 1a-c shows TEM images of SGN-900, SGN-1000, and GN-900 respectively. It may be observed that the macroscopic flakes shown in Figure S1 actually consist of defective graphene arranged as interconnected arrays of graphene nanoboxes with each box having a wall thicknesses in the sub-5 nm range and the average being 3 nm. Figure 1d-f shows the high-resolution TEM (HRTEM) images and the corresponding layer spacing profiles of SGN-900, SGN-1000, and GN-900, respectively. These images further highlight the internal structure of the graphene nanoboxes, demonstrating how increasing deposition (pyrolysis) temperature promotes greater ordering. Per the layer spacing profiles shown below the figures, it may be observed that in all cases the average graphene spacing is larger than 0.3354 nm of graphite. For SGN-900, SGN-1000, and GN-900, the average values are very similar at 0.358, 0.352, and 0.356 nm. Thiophene is a five-membered heterogeneous ring compound containing one sulfur heteroatom. As the carbonization proceeds, sulfur conjugates the graphene layer and expands the layer spacing. Likewise, the oxygen atoms in the alcohol will bind to the graphene and expand its spacing, explaining the layer dilation in GN-900.

Figure 1g-j shows the high-angle annular dark fieldscanning transmission electron microscope (HAADF-STEM) image and the corresponding energy dispersive X-ray spectroscopy (EDXS) mappings of C, O, and S for SGN-900. Per the EDXS maps, both S and O are incorporated into the structure. With increasing carbonization temperature, the border of the cubic nanoboxes becomes more well-defined. The graphene layers in SGN-1000 are more ordered than in SGN-900. With increasing synthesis temperature, the graphene ribbons become longer as well. However, even for SGN-1000, the graphene remains highly defective relative to the graphene present in standard graphite. It is known that the dilated graphene layer spacing promotes more facile K ion intercalation. 47,61 Meanwhile, the defect sites in the carbons will provide sites for reversible K ion adsorption, both near the surfaces and within the bulk.^{6,62} Since SGN-900 and GN-900 are morphologically and structurally analogous, by directly comparing their electrochemical performance, it is possible to understand the role of S-doping in K ion storage.

Figure 2 shows further structural and surface characterization of SGNs and GN. Figure 2a shows XRD patterns with the highly broadened (002) Bragg peak going to higher 2θ values with increasing temperature. For SGN-900 and SGN-1000, the center of the (002) peak shifts from 24.8° to 25.3°, becoming incrementally sharper in the process. For GN-900, the center of the peak is at 24.85°. The calculated mean layer spacing is then 0.358, 0.352, and 0.356 nm, respectively, agreeing in trend with the HRTEM analysis. A qualitative measure of ordering is the *R*-value, defined as (002) peak height normalized by the background intensity. $^{63-65}$ The *R*-

values of SGN-900 and SGN-1000 are 1.88 and 2.17, respectively. For GN-900, the *R*-value is 2.00. This indicates that S causes increased levels of disordering in the carbon structure

Raman spectra for SGNs and GN are shown in Figures 2b and S2. For carbons, the disorder induced D-band is centered at 1345 cm⁻¹, while the graphitic G-band is centered at 1580 cm⁻¹.66 The D-band is associated with the breathing mode of sp² carbon atoms in aromatic rings, while the G-band derives from the conjugated structure in chains or rings of sp² carbon.^{67,68} The T-band located at ~1220 cm⁻¹ can be attributable to impurities or heteroatoms, such as S, on the graphitic plane. The D"-band located at ~1480 cm⁻¹ corresponds to defects in graphene layer stacking.^{69,70} The integral peak intensity ratio of $I_{\rm G}/I_{\rm D}$ can be utilized to assess the defect and disorder level in carbon materials. As shown in Table S1, the intensity ratio increases with increasing pyrolysis temperature, indicating more order. I_G/I_D for SGN-900 and SGN-1000 is 0.94 and 1.12, respectively. For GN-900, $I_{\rm G}/I_{\rm D}$ is 1.25. The value of $I_{\rm D}/(I_{\rm G}+I_{\rm D})$ can also be employed as a measure of defectiveness, ^{71,72} decreasing from 2.06 for SGNmeasure of defectiveness, 900 to 1.89 for SGN-1000. For GN-900, $I_{\rm D}/(I_{\rm G}+I_{\rm D})$ is 1.80. Overall, the HRTEM, XRD, and Raman results are in agreement: Employing the S-rich thiophene precursor leads to an incrementally less ordered graphene-like carbon structure versus the baseline alcohol precursor. As expected, an increase in the pyrolysis temperature from 900 to 1000 °C leads to more ordering.

Electrical conductivity was obtained using four-point probe measurements. The measured values were 152.9, 135.5, and 111.9 S m⁻¹ for SGN-900, SGN-1000, and GN-900, respectively. Despite decreased order, the S-rich carbons had higher electrical conductivity, agreeing with prior reports on the beneficial role of S-doping.⁷³ The evolution of the surface area and pore structure of the SGNs and GN was evaluated by N₂ adsorption. According to Figure 2c, the isotherms show typical type IV curves combined with an H3-type hysteresis loop, demonstrating mesoporosity. ⁷⁴ The Brunauer–Emmett– Teller surface area decreases from 925 m²g⁻¹ for SGN-900 to 395 m²g⁻¹ for SGN-1000. The GN-900 shows a specific surface area of 815 m²g⁻¹, which is close to that of SGN-900. Figure 2d shows the pore size distribution calculated by the non-local density functional theory (NLDFT) model. As the temperature increases, the pore volume decreases from 3.75 cm³g⁻¹ for SGN-900 to 1.96 cm³g⁻¹ for SGN-1000. GN-900 has a pore volume of 3.30 cm³g⁻¹, again relatively on par with

The X-ray photoelectron spectroscopy (XPS) analysis was carried out to investigate the near-surface chemistry in SGN and GN specimens. Figure 2e shows the survey XPS spectra of SGN-900, SGN-1000, and GN-900. Only C, O, and S atoms are detected in SGN-900 and SGN-1000, while only C and O are detected in GN-900. As shown in Figure 2f, the highresolution C 1s spectra of the SGN-900 can be deconvoluted into the dominant C-C/C=C peak at 284.6 eV, along with C-S/C-O at 285.2 eV, C=O at 286.9 eV, and O-C=O at 290 eV, respectively.⁷⁵ The C 1s spectra of GN-900 are shown in Figure S3d and consist of C-C/C=C at 284.6 eV, C-O at 285.4 eV, C=O at 286.7 eV, and O-C=O at 289.5 eV. As seen in Table S1, the S content in SGN-900 and SGN-1000 is 4.30 and 1.93 at. %, respectively. A higher pyrolysis temperature is expected to lead to more elimination of the S from the carbon structure.

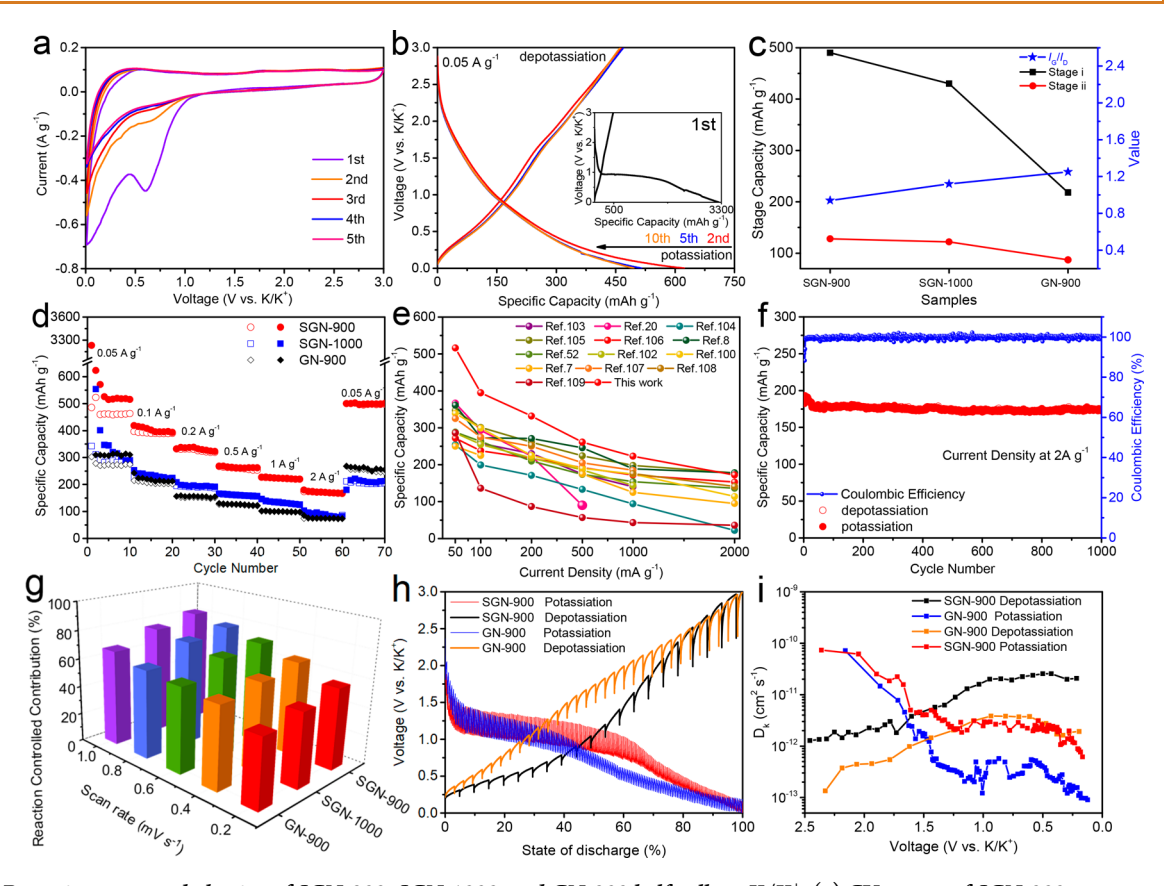


Figure 3. Potassium storage behavior of SGN-900, SGN-1000, and GN-900 half-cells vs K/K*. (a) CV curves of SGN-900 at a scan rate of 0.1 mV s^{-1} . (b) Galvanostatic profiles of SGN-900 at 0.05 A g^{-1} with the inset showing the first cycle. (c) $Stage\ i$ (below 0.1 V vs K/K*) and $Stage\ ii$ (above 0.1 V) capacity, along with the associated Raman I_G/I_D ratio. Capacity data obtained at 0.05 A g^{-1} . (d) Rate performance. (e) Specific capacity comparison of SGN-900 versus state-of-the-art carbon anodes from the literature. (f) Cycling stability of SGN-900 at 2 A g^{-1} . (g) Reaction-controlled contributions of the SGNs and GN at different scan rates. (h) GITT profiles and (i) the corresponding potassium ion diffusion coefficients at various potassiation/depotassiation voltages.

Table S2 compares the previously employed synthesis methods for obtaining S-doped carbons. The most common to obtain S-doping is by physically mixing the carbon precursor with elemental sulfur powder. 12,59,61,73,76-79 During the heating process, the S₈ molecules are cleaved into radicals and can become covalently bonded with the carbon structure. The small sulfur molecules can also become trapped at the carbon defects or in the nanopores. Benzyl disulfide, phenyl disulfide, and sulfate salt have also been employed as the precursors for the introduction of sulfur into carbon. 9,75,80-84 In the case of elemental S or the prior precursors, sufficient sulfur-doping is only maintained with a relatively low carbonization temperature (e.g., <800 °C). This is because these precursors are otherwise eliminated before reacting with the carbon, e.g., elemental S sublimation. Because of the low pyrolysis temperatures, the obtained carbons are amorphous rather than ordered and graphene-like. Thiophene, the precursor employed in this study, possesses a thermally stable structure relative to other S-containing organic molecules.85 During the 900 or 1000 °C pyrolysis, thiophene's strong carbon-sulfur bond causes much of the S to be retained in the final product. Meanwhile, thiophene's aromatic structure leads to the high degree of ordering (graphitization), making it in effect a "soft carbon" precursor analogous to various S-free aromatic molecules.86

The high-resolution S 2p spectra of SGN-900 and SGN-1000 (Figures 2g and S3b) can be deconvoluted in two strong

peaks at around 163.8 eV/165.0 eV and another two weak peaks at 167.7 eV/169.4 eV. These correspond to thiophenetype S (strong chemical S-S/C-S bonds) and oxidized-type S.⁷⁵ The O 1s spectra are shown in Figure 2h. The peaks can be fitted into four components: O-S at 531.4 eV, C=O at 532.4 eV, C-O-C/C-OH at 533.2 eV, and a -COOH bond at 534.0 eV. 87 The O 1s spectrum of GN-900 shown in Figure S3e displays C=O at 532.1 eV, C-O-C/C-OH at 533.1 eV, and -COOH at 534.2 eV, respectively. Atomic percentages of various S and O functional groups in SGN-900, SGN-1000, and GN-900 are presented in Figure S4 and Table S3. The relative surface concentration of covalent sulfur S 2p1/2 functional groups of SGN-900 is 26%, which is higher than the 25% in SGN-1000. SGN-900 contained 56% O-S functional groups, while SGN-1000 contained 50% of these groups.

To further understand the role of S in the electrochemical performance of the carbons, we prepared another baseline specimen. The sample SGN-900-1200 was obtained by annealing SGN-900 at 1200 °C for 2 h in nitrogen. The associated results are presented in Table S1 and in Figure S5. The SEM and TEM analyses show that the overall morphology of SGN-900-1200 is analogous to SGN-900. However, SGN-900-1200 exhibits a higher degree of graphene ordering as indicated by the XRD, Raman, and HRTEM analyses with a relatively smaller graphene spacing of 0.351 nm and a relatively higher $I_{\rm G}/I_{\rm D}$ of 1.17. Moreover, SGN-900-1200 displays

decreased surface area and pore volume. Due to the high-temperature calcination, the S atoms escape from the carbon structure ^{86,87} with the ultimate S content of SGN-900-1200 being at 1.25 at. %.

Electrochemical Performance of SGNs in Potassium **Ion Batteries/Capacitors.** The electrochemical performance of SGN-900, SGN-1000, and the baseline GN-900 was investigated as half-cell potassium ion anodes vs K/K+, employing 0.8 M KPF₆ in EC-DEC (1:1, v/v) as the electrolyte. The cyclic voltammetry (CV) curves for SGN-900 at scan rate of 0.1 mV s⁻¹ are shown in Figure 3a. The CV curves for the rest of the carbons are shown in Figure S6. For all the samples, at the initial potassiation cycle, there is a prominent cathodic peak initiating near 1 V (and centered near 0.6 V) with no anodic counterpart. This irreversible cathodic peak occurs due to the formation of the solid electrolyte interphase (SEI) on the relatively high surface area of each of the carbons. In addition, there is a contribution from irreversible trapping of K ions at some high energy graphene defect sites. 79 The irreversible capacity due to the 0.6 V peak decreased from SGN-900 to SGN-1000. This is due to both a lowering of the electroactive surface area and a reduction of carbon defect density with increasing pyrolysis temperature. In the subsequent cycles, the carbons display a nondescript shape to the CV with the associated charge storage mechanisms being discussed shortly. It may be observed that the area of the CV curve for the GN-900 electrode is substantially lower than for the SGN-900 and SGN-1000 electrodes. The higher reversible current with SGN-900 and SGN-1000 versus GN-900 is directly attributable to the presence of S and the associated defects in the structure.

Figure 3b displays the galvanostatic curves for SGN-900, while Figure S6 displays them for SGN-1000 and GN-900. Tested at 0.05 A g^{-1} , the cycle 1 reversible depotassiation capacities for SGN-900, SGN-1000, and GN-900 are 485, 340, and 300 mAh g⁻¹, respectively. The large irreversible sloping plateau at the first potassiation is primarily due to the SEI formation. The initiation of this sloping plateau at ~1 V agrees with the CV results. Because of the large surface area of these materials and the associated SEI, the first cycle Coulombic efficiency (CE) is relatively low. The cycle 1 CE values for SGN-900 and SGN-1000 are 15.5% and 20.3%, respectively. The cycle 1 CE for GN-900 is 10.9%. It should be pointed out that such cycle 1 CE values are expected for carbons with a high surface area tested against K/K⁺, being on-par with what has been previously reported for K storage. In general, K-based electrolyte systems are immature, leading to excessive SEI growth on a range of anodes. 13,88 Such an extensive SEI formation and a corresponding low CE are prevalent for "graphene-like" structures across the spectrum K ion publications.

To further support this point, Table S4 presents the compiled initial CE results for state-of-the-art high surface area K ion carbons from the literature. ^{7,8,34,52,57,89–99} It may be observed that the 15–20% cycle 1 CE is on par with prior publications. In the subsequent cycles, the galvanostatic profiles are monotonically decreasing/increasing at potassiation/depotassiation. As will be demonstrated by a combination of XPS and HRTEM analyses, the higher voltage—capacity originates from the reversible adsorption of K ions at structural and chemical defect sites in the carbons. The low voltage reversible capacity also contains a contribution from the reversible K ion intercalation, in addition to ion adsorption.

Recently, Wu's group reported that the concentrated potassium bis(fluorosulfonyl)imide (KFSI) in dimethoxyethane (DME)-1,1,2,2-tetrafluoroethyl-2,2,2-trifluoroethyl ether (HFE) (1:1.90:0.95 by mol) electrolyte can be used for improving the initial CE of graphite.²⁸ Inspired by this discovery, we tested the electrochemical performance of SGN-900 using KFSI in DME-HFE electrolyte. These results are shown in Figure S7. Tested at 0.05 A g-1, the cycle 1 potassiation and depotassiation capacities are 1880 and 678 mhA g⁻¹, respectively. A CE of 36.1% is a significant improvement over the carbonate electrolyte results, demonstrating the key role of new electrolyte formulations in optimizing PIB performance. The substantially improved initial CE indicates that the associated SEI is more passivating and is relatively thinner, consuming less potassium ions in its formation.

The potassiation mechanisms in SGN and GN may be subdivided into a monotonic region above 0.1 V vs K/K⁺ and a sloping plateau region below 0.1 V. The region above 0.1 V vs K/K^+ may be termed Stage i, while that below 0.1 V may be termed Stage ii. The separation at 0.1 V is somewhat arbitrary but is useful in providing a discussion of the distinct storage mechanisms. Figure 3c plots the capacity contribution to Stage i and Stage ii for SGN-900, SGN-1000, and GN-900 along with the Raman I_G/I_D ratio in each carbon. The numbers in Figure 3c were obtained from the second cycle potassiation, tested at a relatively low current density of 0.05 A g⁻¹. Figure S8 directly compares the second cycle potassiation profiles in the three carbons, which is the source of the data for Figure 3c. The capacity achieved at Stage i has been ascribed to the reversible K ion adsorption at chemical-structural defects within the surface and the bulk of nongraphitic carbons. 100,101 The capacity achieved at Stage ii can be due to reversible K ion intercalation, given that intercalation is feasible into a given structure. 47,100,102 With conventional graphite tested against K/K+, Stage ii would be the vast majority of the capacity. For disordered carbons, Stage ii capacity would depend on the ease of K ion intercalation with more ordered and more (002) dilated carbons being favored. Stage i capacity for SGN-900 and SGN-1000 is 490 and 430 mAh g⁻¹, agreeing with the trends in the heteroatom content in these materials. Notably, Stage i capacity for GN-900 is much lower, being 218 mAh g⁻¹. The key difference between SGN-900 and GN-900 is the S content, which is 4.30 at. % versus nil. For SGN-900 and GN-900, the $I_{\rm C}/I_{\rm D}$ ratios are 0.94 and 1.25, supporting the greater defectiveness in the former due to S. This gives direct evidence to the contribution to the reversible high-voltage capacity from the chemically bound sulfur species in the carbons and the associated defects.

The capacity at *Stage ii* has been attributed to the intercalation of potassium ions between the defective graphene layers.⁴⁴ However, we believe that reversible ion adsorption is active in this region as well. This is due to both the trends in the *Stage ii* capacities and the results of XPS analysis presented in the next sections: Despite a substantial difference in the degree of graphene order in the carbons, their *Stage ii* capacity is similar. In fact, there is an opposite trend in terms of *Stage ii* capacity versus Raman, HRTEM, and XRD-indicated ordering. For SGN-900, SGN-1000, and GN-900, *Stage ii* capacities are 128, 122, and 87 mAh g⁻¹, respectively. The XRD calculated mean layer spacing for SGN-900, SGN-1000, and GN-900 is 0.358, 0.352, and 0.356 nm. This means that all three carbons display comparable graphene layer dilation relative to that in

graphite. The GN-900 specimen is actually more ordered than SGN-900, while also possessing an expanded graphene layer distance. Yet, despite this, it stores less K ions below 0.1 V than its S-containing counterpart. The GN-900 specimen stores overall less K ions than SGN-900 at all currents tested and throughout the entire voltage range. This gives direct evidence to the contribution to the reversible low-voltage capacity from the chemically bound sulfur species. As will be demonstrated by HRTEM, reversible K ion intercalation does occur below 0.1 V. However, per these electroanalytical results combined with XPS, intercalation is not the exclusive contributor to the capacity in this voltage range.

The electrodes were rate tested at currents ranging from 0.05 to 2 A g⁻¹ as shown in Figure 3d. It may be observed that SGN-900 delivers an excellent rate performance with a stable capacity ranging from 516 mAh g⁻¹ at 0.05 A g⁻¹ to 172 mAh g⁻¹ at 2 A g⁻¹. When the current density was reduced back to 0.05 A g⁻¹, a capacity of 500 mAh g⁻¹ was recovered, indicating little damage to the structure due to the high rate tests. Both SGN-1000 and GN-900 display lower capacity at all rates, demonstrating the need for S and the defects in the fast charge performance. SGN-900 displays a favorable reversible capacity throughout a wide range of currents, relative to the state-of-the-art potassium ion anodes from the literature, including carbon- and oxide-based systems. ^{7,8,20,52,100,102–109} This is illustrated in Figure 3e and in Table S5, where a wide range of K ion anodes is directly compared in terms of their electrochemical performance at a comparable mass loading.

SGN-900 shows excellent stability during cycling (Figure 3f). When tested at 2 A g⁻¹, the cycle 1 and cycle 1000 reversible capacities are 193 and of 172 mAh g⁻¹ (0.011% capacity decay per cycle) with a cycling CE of >99%. The vast majority of the capacity decay occurs during the initial 30 cycles. The capacity loss between 31 and 1000 cycles is only 0.0033% per cycle. The thin carbon walls will reduce the ion diffusion lengths, while being elastically compliant enough to allow the necessary volume expansion/contraction without structural damage. Such reversible dilation-contraction will be illustrated by ex situ TEM analysis, shown next. The SGN-900-1200 sample, containing only 1.25 at. %, displays a capacity of 300 mAh g^{-1} at 0.05 A g^{-1} and 133 mAh g^{-1} at 2 A g^{-1} . It shows 68% capacity retention after 1000 cycles at 2 A g⁻¹ (Figure S9), which is inferior to that of SGN-900. Therefore, S-doping is considered important not only for the overall reversibly capacity and rate performance but also for cyclability.

The kinetic behavior of SGN-900 and GN-900 was further analyzed by CV analysis at scan rates of 0.2 to 1.0 mV s⁻¹. These results are shown in Figure S10. The charge storage mechanisms in the carbons are reaction controlled or diffusion controlled, depending on the voltage and the scan rate. The relationship between the peak current (i) and the scan rate (ν) may be generally expressed by eq 1:

$$i = av^b (1)$$

where a and b are both adjustable parameters. The value of the parameter b can be obtained from the slope of the plot of log (i) versus log (v). When the b value approaches 1, indicating a linear relationship of peak current with time, the charge storage process is taken to be interfacial reaction limited. For anode materials that are covered by an SEI layer, this so-called "capacitive-controlled" process is not the classical surface, only the EDLC charge storage mechanism. The electrode's

surface area is not sufficient to generate appreciable EDLC current. For SEI-covered carbon anodes, the reaction-controlled charge storage capacity can originate from bulk and surface reversible ion adsorption at the structural and chemical defects. When the *b* value approaches 0.5, charge storage mechanisms are solid-state diffusion controlled. For graphite, this is the classic staged intercalation process. For the substantially more disordered carbons, such as SGN-900, both bulk intercalation and bulk ion adsorption may be diffusion limited. Per Figure S10b using the cathodic/anodic references of 0.01 and 0.3 V, the calculated *b* values were 0.64 and 0.66, respectively. This indicates that the low voltage—capacity is solid-state diffusion controlled. When the references of 0.75 and 1.8 V are considered, the resulting *b* values are closer to reaction controlled, being 0.86 and 0.83.

The relative contribution to the total capacity from the reaction-controlled versus the diffusion-controlled ion storage process can be further evaluated according to eq 2:

$$i = k_1 v + k_2 v^{1/2} (2)$$

where $k_1 \nu$ and $k_2 \nu^{1/2}$ represent the reaction-controlled contribution and the solid-state diffusion-controlled contribution. 112 At a set voltage, a given charge storage mechanism is either reaction controlled or diffusion controlled but not both. However, as the voltage is swept from its maximum to its minimum, the same mechanism may change in its rate limiting step. The same may occur with a change in scan rate. Figures 3g and S11 show the results of this analysis for SGN-900, SGN-1000, and HNC-900, showing the relative contribution to the total capacity in percent. It may be observed that, at each scan rate, the relative contribution from reactioncontrolled capacity increases with S and defect content. SGN-900 is the most S and defect rich and yields the highest reaction controlled percentage, up to 82% at 1 mV s⁻¹. GN is the most ordered and is S-free, yielding 67% at 1 mV s⁻¹, while SGN-1000 yields 76% at 1 mV s⁻¹. From Table S6, it may be observed that SGN-900 is superb in the published literature in terms of the degree by which its capacity contribution is reaction dominated, supporting the rate capability comparison presented in Figure 3e. This again highlights the role of sulfur and the associated defects, since SGN-1000 and GN-900 are more balanced between reaction and diffusion controlled.

To further understand the kinetics of potassium storage in these materials, galvanostatic intermittent titration technique (GITT) measurements were performed on SGN-900 and GN-900. This allowed one to calculate the diffusion coefficient (Dk) as a function of voltage, during both potassiation and depotassiation. The details of the analysis, including the additional plots and descriptions, are presented in Figure S12. The voltage response of both materials and the calculated D_k values at differing potassiation/depotassiation depths are shown on Figure 3h,i. For both carbons, the D_k decreases with potassiation depth, which may be attributed to increased site occupancy and decreased driving force for additional ion insertion. During depotassiation, the trend is reversed, with maximum diffusivity being at the onset voltage of ion extraction. The ion sites that have the least driving force for insertion (lowest voltage) offer the most facile extraction kinetics. The D_k values for SGN-900 range from 10^{-10} to 10^{-12} cm² s⁻¹, an order of magnitude higher than the 10^{-11} to 10^{-13} cm² s⁻¹ values for GN-900. This significant difference in diffusivities is due to the S content in SGN-900, since otherwise the two carbons possess an analogous structure. The

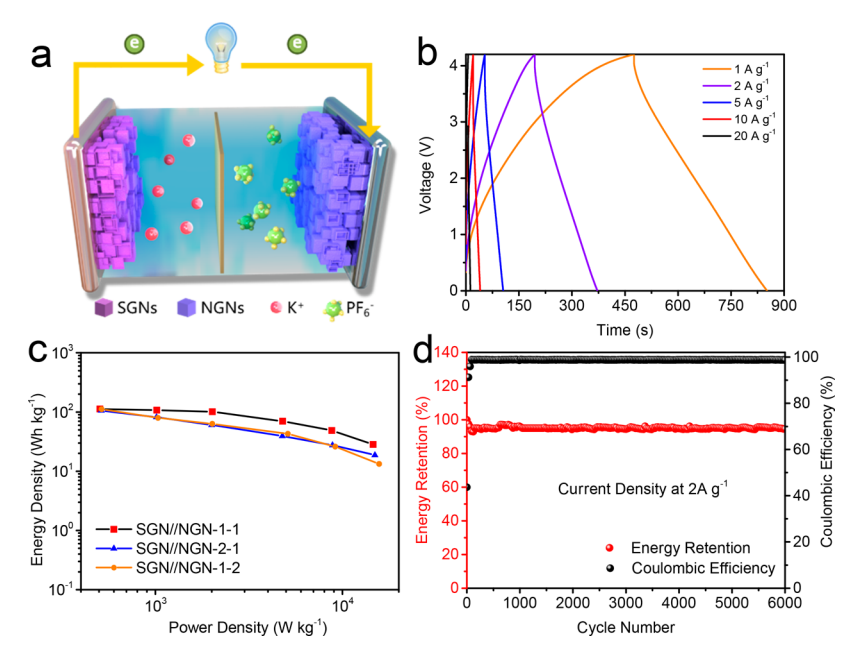


Figure 4. Electrochemical performance of a potassium ion capacitor based on a SGN-900 anode and a NGN cathode. (a) Schematic diagram illustrating the asymmetric PIC design. (b) Galvanostatic charge—discharge profiles with the anode to cathode mass ratio of 1:1. (c) Ragone plots of the PICs with different mass ratios of anode to cathode (1:2, 1:1, and 2:1). (d) Cycling stability of the PIC tested at 2 A g⁻¹.

diffusivities in turn explain the superior fast charge capability of SGN-900 and the associated dominance of reaction-controlled kinetics. GITT analysis was also employed to analyze SGN-900 and GN-900 at cycle 2, as shown in Figure S13. The derived $D_{\rm k}$ values display the same trend as during the first cycle. Moreover, the $D_{\rm k}$ values also range from 10^{-10} to 10^{-12} cm² s⁻¹, demonstrating consistent potassium diffusivity at both cycles.

Electrochemical impedance spectroscopy (EIS) was used to further analyze the electrochemical performance of the SGNs and GNs. Figure S14 compares the Nyquist plots of SGN-900 and GN-900 prior to cycling at OCP and after 500 cycles at 1 A g⁻¹ in the depotassiated state. All the plots consist of a semicircle at the high frequency region and a sloping line at the low frequency region. The semicircle is related to a combination of SEI resistance $R_{\rm SEI}$ and charge transfer resistance $R_{\rm CT}$. In principle, these should be distinct overlapping semicircles, the SEI resistance being at the higher frequency. In many cases including here, the circles sufficiently overlap so that they cannot be mathematically deconvoluted. The R_(SEI+CT) values for SGN-900 and GN-900 are 288 and 450 Ω , respectively. This indicates that the S-free GN-900 has incrementally higher impedance from the onset. The Warburg factor σ can be calculated from the low frequency region of the Nyquist plots; the details are found in the Supporting Information. The linear relationship between Z' and $\omega^{-1/2}$ (ω is the angular frequency) of SGN-900 and GN-900 is shown in Figure S14. The calculated values of σ for pristine SGN-900 and GN-900 are 42.0 and 109.8. The lower σ value for SGN-900 also indicates a higher diffusion coefficient. The post cycled $R_{(SEI+CT)}$ values for SGN-900 and GN-900 are 1827 and 2553 Ω , as shown in Figure S14.

To further investigate the fast-rate K ion storage performance of SGN-900, potassium ion capacitors were fabricated by using SGN-900 as the anode and the nitrogen-rich graphene nanobox NGN-900 as the cathode. The high nitrogen content in NGN-900 (9.2 at. %) is beneficial for improving the high

voltage-capacity needed for the cathode, while the mesoporous structure facilitates transport. The SGN//NGN PIC architecture is schematically illustrated in Figure 4a. The preparation process of NGN-900 is provided in the Supporting Information. Figure S15a shows the SEM and TEM (inset) images of NGN-900. Figure S15b shows the representative galvanostatic charge-discharge profiles of NGN-900 tested at 0.1 A g⁻¹. Figure S15c shows this rate performance for the NGN-900 sample. Within the cathode voltage range of 2-4.2 V vs K/K+, NGN-900 achieved a specific capacity of 60 mAh g^{-1} at 0.2 A g^{-1} and 30 mAh g^{-1} at 10 A g^{-1} . Prior to being assembled into a PIC, the SGN-900 anode was "activated" by being cycled three times in a half-cell vs K/K⁺ at 0.05 A g⁻¹ to a cutoff voltage of 3 V, leaving in the depotassiated state but with a stable SEI. Since neither electrode contained a K reservoir, during testing, the cations and anions are derived from the electrolyte only.

To obtain the best electrochemical performance, the mass ratio between SGN-900 and NGN-900 was optimized. Three mass ratios of 1:2, 1:1, and 2:1 were investigated with the working window of SGN//NGNs being set at 0-4.2 V. According to Figures S16 and 4b, the CV and galvanostatic curves of PICs are not ideal "EDLC-like" triangles; i.e., they are not pseudocapacitive. This is due to the combined storage mechanism discussed previously. As illustrated in Figure 4c, the PIC device with a mass ratio of 1:1 displays the optimum energy and power combination. The specific energy (E, Wh kg⁻¹) and specific power (P, W kg⁻¹) are calculated by the following standard equations of $P = i\Delta V/m$ and $E = P\Delta t$, where i is the discharge current, ΔV is the average voltage (excluding the IR drop), m is the total loading of active materials (anode and cathode), and Δt is the discharge time. The PIC with anode to cathode mass ratio of 1:1 delivers an energy of 112 Wh kg^{-1} at a power of 505 W kg^{-1} and 107, 100, 70, 49, and 28 Wh kg^{-1} at 1, 2, 4.8, 8.8, and 14.6 kW $kg^{-1}.$ As shown in Figure 4d, the energy retention of this device is 92% after 6000 cycles at 2 A g⁻¹ with cycling CE over 99%. Table

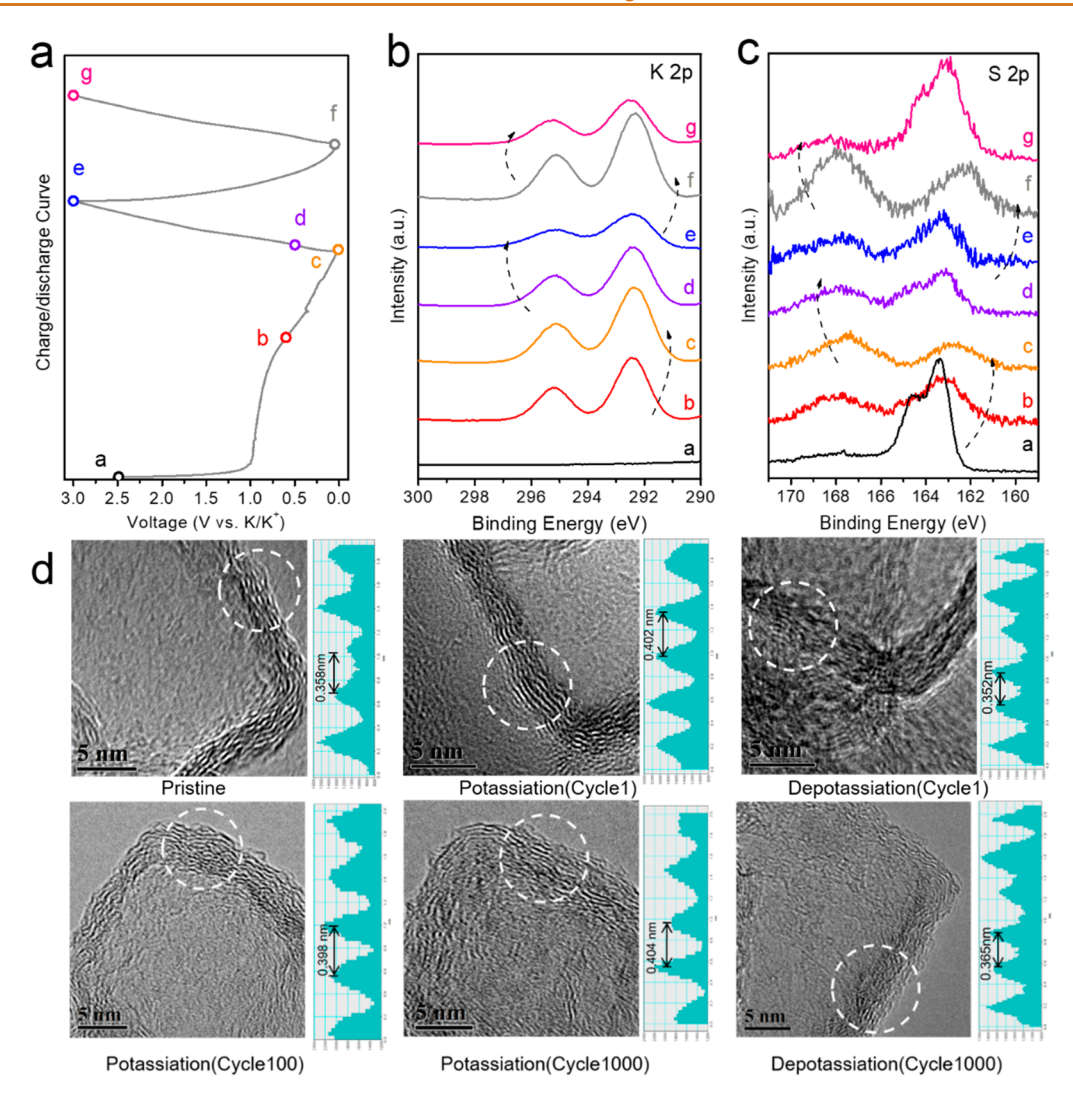


Figure 5. Post-mortem XPS and HRTEM analysis of SGN-900 at different potassiation/depotassiation states. (a) The potassiation/depotassiation voltage profiles at cycle 1 and cycle 2, including points at which the test was interrupted and the cells were disassembled for analysis. Corresponding high resolution (b) K 2p and (c) S 2p spectra. (d) HRTEM images and the corresponding graphene layer spacing of SGN-900 at states of as-synthesized, after terminal potassiation to 0.001 V at cycle 1 (0.05 A $\rm g^{-1}$), after terminal depotassiation to 3.0 V at cycle 100 (2 A $\rm g^{-1}$), after terminal potassiation to 3.0 V at cycle 1000 (2 A $\rm g^{-1}$), and after terminal depotassiation to 3.0 V at cycle 1000 (2 A $\rm g^{-1}$).

S7 shows energy, power, and characteristics of related prior art, demonstrating the highly favorable energy, power, and cyclability characteristics of the SGN//NGN PICs.

Investigation of the Potassium Storage Mechanism in SGNs. To further understand the potassium storage mechanisms in SGN-900, post-mortem XPS analysis was performed at different cutoff voltages during potassiation and depotassiation. These results are shown in Figures 5 and S17. The K 2p spectra for these potassiation states are shown in Figures 5b and S18. Per points a-c, the two peaks located at 292.4 and 295.2 eV during the potassiation process indicate the formation of K-C bonds, likely being formed at the carbon structural defects. When the potassiation process proceeds to 0.6 V vs K/K+, the above two peaks shift to a lower binding energy $(E_{\rm b})$, while increasing in overall intensity. At 0.001 V, these peaks shift to the lowest binding energy while achieving their maximum intensity. At the lower voltages, there is K ion intercalation between the defective graphene sheets, which will be further supported by the HRTEM analysis shown next. During the subsequent depotassiation process, the two peaks

recover to higher $E_{\rm b}$ values while reducing in their intensity. At the end of the first depotassiation process (point e), the two peaks still exist albeit at a much lower intensity. This is associated with the irreversible insertion of K into the most strongly binding defect sites in the carbon host. The XPS peak related to K–F bonds is present at around 292.5 and 295.5 eV, indicating that the SEI layer contains inorganic KF, agreeing with the prior analysis. A comparable trend in energy shifts and intensities is observed during the second potassiation/depotassiation cycle. These largely reversible changes in $E_{\rm b}$ indicate that the potassiation reactions with the carbon matrix are reversible, agreeing well with the electrochemical results.

The XPS S 2p spectra are shown in Figures 5c and S19. The S 2p peak at the pristine stage can be divided into four peaks at 163.8, 165.0, 167.7, and 169.4 eV, respectively. These correspond to the S $2p^{3/2}$, S $2p^{1/2}$, and sulfate chemical bonds. As the SGN electrode is gradually potassiated to 0.001 V, the two peaks centered at 162.2 eV emerge. These correspond to the K_2S compound, ⁵⁹ which is the equilibrium

terminal phase between K and S. In the fully potassiated state, the $E_{\rm b}$ of S 2p negatively shifted to a lower value, indicating that the strong interaction of K and S atoms lead to a lower valence state of the S. During the depotassiation process to 0.5 V, the intensity of sulfides and sulfates both decreased, and the intensity of the S peaks increased. At 3 V, the $E_{\rm b}$ of S 2p^{3/2} and S 2p^{1/2} shifts to 163.3 and 164.4 eV, indicating a reversible variation of the S valence state. The peak at 162.5 eV can be assigned to the residual sulfide species (S²⁻), which would arise from the incomplete oxidation reaction. The peak at around 165.5 eV can be attributed to K_2SO_4 . At cycle 2, the changes in the S 2p peaks follow the same trend as at cycle 1, indicating largely reversible reactions.

As displayed in Figure S20, the O 1s spectrum of pristine SGNs can be fitted into four peaks: O-S at 531.4 eV, C=O at 532.4 eV, C-O-C/C-OH at 533.2 eV, and -COOH at 534.0 eV. At the potassiated state of 0.6 V, a peak at 532.7 eV can be assigned to K₂CO₃, which is a key component of the SEI. After its formation, the K₂CO₃ peak changes minimally with voltage, indicating the irreversible process of inorganic SEI formation. 113 The C 1s spectra shown in Figure S21 further confirm the existence of K₂CO₃ and other K-organic matter. During the potassiation process, the O-S peaks become slightly stronger, which is consistent with the variation of sulfates. In the following depotassiation process, the intensity of O-S peaks decreased, also indicating the reversible reaction related to S. The relatively strong O-C=O peaks at 289.2 eV can be observed in the potassiated samples, agreeing with the K₂CO₃ bonding. 114 The intensity of C-C/C=C and C-S/C-O peaks dramatically decreases during potassiation, accompanied by the emergence of two pronounced K 2p peaks in the fully potassiated state. These changes have been previously attributed to the reversible formation of the K-S-C compounds. 115 After depotassiation, the C-C/C=C and C-S/C-O peaks become intense again, indicating a reversible reaction.

To obtain further insight regarding the potassium ion storage mechanisms, HRTEM analysis was performed on SGN-900 in the as-synthesized condition, after terminal potassiation to 0.001 V, and after terminal depotassiation to 3.0 V at cycle 1. These results are shown in Figure 5d. Before potassiation, the graphene layer spacing of SGN-900 is 0.358 nm. After potassiation to 0.001 V, the graphene layer spacing is expanded to 0.402 nm, agreeing with K ion intercalation as a secondary charge storage mechanism. However, this layer expansion of about 13% is much less than the 61% dilation in graphite upon the formation of the terminal intercalation compound KC8. In the fully depotassiation state, the layer spacing is reduced to 0.352 nm, indicating the reversibility of the process. Importantly, the hollow graphene structures retain their integrity during cycling. Per the SEM analysis shown in Figure S22, even after 100 and 1000 cycles at 2 A g⁻¹, the overall morphology of SGN-900 is intact. Per the HRTEM results shown in Figure 5d, after 100 and 1000 cycles, the graphene layer spacing of SGN-900 in its potassiated state is 0.398 and 0.404 nm, respectively. After 1000 cycles, the spacing in the depotassiated state is back to 0.365 nm, further confirming the structural integrity and highly reversible intercalation/deintercalation.

CONCLUSIONS

To summarize, we created sulfur-rich graphene nanoboxes (SGNs) synthesized through a facile chemical vapor deposition

method with thiophene as the precursor. A similar approach using an alcohol precursor was employed to fabricate sulfurfree graphene nanoboxes tested as baselines. Employed as K ion anodes, the SGNs show record reversible capacity and record fast charge performance, whereas the sulfur-free baselines are generally midrange. A potassium ion capacitorbased SGN anode and a nitrogen-doped carbon nanobox cathode, without a secondary K reservoir apart from the electrolyte, show outstanding energy, power, and cyclability characteristics. Detailed electroanalysis combined with XPS and HRTEM is employed to elucidate the charge storage mechanisms. The analysis highlights the dominance of the reversible ion adsorption and concomitant reaction with S moieties, combined with limited ion intercalation at low voltages. The covalently bonded S also boosts solid-state diffusivity of K ions by an order of magnitude and stabilizes the SEI structure during the initial potassiation and during cycling.

METHODS

Material Synthesis of SGNs. Commercially purchased magnesium carbonate hydroxide pentahydrate (4MgCO $_3$ ·Mg(OH) $_2$ ·SH $_2$ O, Alfa) was converted into MgO, which was employed as the template for the growth of SGNs. In a typical procedure, 2 g of 4MgCO $_3$ ·Mg(OH) $_2$ ·SH $_2$ O was loaded in a horizontal alumina tube. The tube furnace was heated to the target temperature (900 or 1000 °C) at a ramp rate of 5 °C under a N $_2$ atmosphere. Once the target temperature was achieved, the thiophene vapor was introduced into the tube furnace by bubbling flowing nitrogen through thiophene liquid, and the reaction was maintained for 3 h. The template was removed by washing in 6 M HCl solution for 24 h and then washing with deionized water until the pH was approximately 7. Finally, the samples were freeze-dried and collected. The yield was controlled by adjusting the gas flow for bubbling. For comparison, GNs were synthesized at 900 °C by using ethyl alcohol as the precursor instead of thiophene.

Materials Characterization. The morphologies and microstructures of the SGNs and GNs were characterized by XRD (BrukerD8 Advance powder diffractometer (Cu K α radiation)), SEM (Hitachi S4800, 15 kV), and TEM (JEOL 2010F, 200 kV). Raman spectra were recorded by using a micro-Raman spectroscope (LabRAM HR Evolution) with the excitation wavelength of 532 nm. The surface element analyses of SGNs and GNs were examined on an XPS (Thermo ESCALAB 250XI). The specific area and pore volume were conducted from the nitrogen adsorption/desorption isotherms measured on a Micrometrics Tristar 3020 II at 77 K.

Electrochemical Testing. The electrochemical performance was investigated in coin-type half-cells (CR2032) assembled in a glovebox filled with Ar. The working electrode was fabricated by mixing SGNs/ GNs, acetylene black, and carboxyl methylated cellulose (CMC) in a mass ratio of 75:15:10. A small quantity of ~20% aqueous alcohol was employed to form a slurry, which was coated on a copper foil. The ascoated electrodes were dried at 70 °C for 12 h in vacuum, with the average mass loading of the active material being about 1 mg cm⁻². A potassium foil was used as the counter electrode; a polyethene membrane was employed as the separator, and 0.8 M KPF₆ in EC and DEC (1:1, v/v) was employed as the electrolyte. The CV curves and EIS plots were measured on a Gamry Interface 1000 electrochemical workstation. Galvanostatic data was obtained using a LAND CT2001A battery system. The GITT was performed at a current density of 0.05 A g^{-1} for 30 min followed by a relaxation period of 3 h. For the electrochemical testing of the potassium ion capacitors, the cathode formulation consisted of 75 wt % NGN-900, 15 wt % acetylene black, and 10 wt % CMC. These were mixed in 20%aqueous alcohol and coated on a stainless foil. After that, the cathode was dried at 70 °C under vacuum overnight.

ASSOCIATED CONTENT

Supporting Information

The Supporting Information is available free of charge at https://pubs.acs.org/doi/10.1021/acsnano.0c09290.

SEM images of all samples; fitted Raman spectra; table of physical and textural properties of all samples; XPS spectra and the related XPS analysis results; table of the sulfur content compared with different synthesis processes; relative surface concentrations; table of XPS analysis results; SEM images, TEM image, XRD pattern, Raman spectrum, nitrogen adsorption-desorption isotherm curves, and survey spectra; CV and galvanostatic charge-discharge profiles for all samples; table of the comparison of initial CE with previously reported carbons; electrochemical measurement of SGN-900 in KFSI electrolyte; second potassiation curves; table of the electrochemical performance compared with previously reported anodes; kinetics analysis of the samples; GITT analysis; Nyquist plots; CV curves of PICs; table of the comparison with the performance of previously reported PICs; ex situ XPS analysis of the SGN-900 sample; postmortem SEM images of SGN-900 (PDF)

AUTHOR INFORMATION

Corresponding Authors

Huanlei Wang — School of Materials Science and Engineering, Ocean University of China, Qingdao, Shandong 266100, People's Republic of China; ⊙ orcid.org/0000-0001-8218-1762; Email: huanleiwang@gmail.com

David Mitlin — Walker Department of Mechanical Engineering, The University of Texas at Austin, Austin, Texas 78712-1591, United States; orcid.org/0000-0002-7556-3575; Email: david.mitlin2@utexas.edu

Authors

Yiwei Sun — School of Materials Science and Engineering, Ocean University of China, Qingdao, Shandong 266100, People's Republic of China; orcid.org/0000-0002-0815-1861

Wenrui Wei − School of Materials Science and Engineering, Ocean University of China, Qingdao, Shandong 266100, People's Republic of China; orcid.org/0000-0002-3132-8354

Yulong Zheng — School of Materials Science and Engineering, Ocean University of China, Qingdao, Shandong 266100, People's Republic of China; ⊚ orcid.org/0000-0001-6944-2737

Lin Tao – School of Materials Science and Engineering, Ocean University of China, Qingdao, Shandong 266100, People's Republic of China; orcid.org/0000-0001-6392-5789

Yixian Wang — Walker Department of Mechanical Engineering, The University of Texas at Austin, Austin, Texas 78712-1591, United States; orcid.org/0000-0001-6107-

Minghua Huang — School of Materials Science and Engineering, Ocean University of China, Qingdao, Shandong 266100, People's Republic of China; orcid.org/0000-0002-9622-3131

Jing Shi – School of Materials Science and Engineering, Ocean University of China, Qingdao, Shandong 266100, People's Republic of China; orcid.org/0000-0002-1309-5606 Zhi-Cheng Shi — School of Materials Science and Engineering, Ocean University of China, Qingdao, Shandong 266100, People's Republic of China; ⊙ orcid.org/0000-0002-5001-1862

Complete contact information is available at: https://pubs.acs.org/10.1021/acsnano.0c09290

Notes

The authors declare no competing financial interest.

ACKNOWLEDGMENTS

Y.S., H.W., W.W., Y.Z., L.T., M.H., J.S., and Z.-C.S. (conception of research, synthesis and experimental analysis, copreparation of manuscript) were supported by the Shandong Provincial Key R&D Plan and the Public Welfare Special Program, China (2019GGX102038), the Fundamental Research Funds for the Central Universities (Nos. 201822008 and 201941010), the Qingdao City Programs for Science and Technology Plan Projects (19-6-2-77-cg), the National Natural Science Foundation of China (Nos. 21775142 and 21471139), and the Sino-German Center for Research Promotion (Grants GZ 1351). D.M. and Y.W. (conception and guidance of research, preparation of manuscript) were supported by the National Science Foundation, Civil, Mechanical and Manufacturing Innovation (CMMI), Award Number 1911905.

REFERENCES

- (1) Xiao, P.; Li, S.; Yu, C.; Wang, Y.; Xu, Y. Interface Engineering between the Metal—Organic Framework Nanocrystal and Graphene toward Ultrahigh Potassium-Ion Storage Performance. *ACS Nano* **2020**, *14*, 10210—10218.
- (2) Xiong, P.; Wu, J.; Zhou, M.; Xu, Y. Bismuth–Antimony Alloy Nanoparticle@Porous Carbon Nanosheet Composite Anode for High-Performance Potassium-Ion Batteries. *ACS Nano* **2020**, *14*, 1018–1026.
- (3) Zhang, Z.; Jia, B.; Liu, L.; Zhao, Y.; Wu, H.; Qin, M.; Han, K.; Wang, W. A.; Xi, K.; Zhang, L.; Qi, G.; Qu, X.; Kumar, R. V. Hollow Multihole Carbon Bowls: A Stress-Release Structure Design for High-Stability and High-Volumetric-Capacity Potassium-Ion Batteries. *ACS Nano* **2019**, *13*, 11363–11371.
- (4) Chou, S.; Yu, Y. Next Generation Batteries: Aim for the Future. *Adv. Energy Mater.* **2017**, *7*, 1703223.
- (5) An, Y.; Tian, Y.; Ci, L.; Xiong, S.; Feng, J.; Qian, Y. Micron-Sized Nanoporous Antimony with Tunable Porosity for High-Performance Potassium-Ion Batteries. *ACS Nano* **2018**, *12*, 12932–12940.
- (6) Tao, L.; Yang, Y.; Wang, H.; Zheng, Y.; Hao, H.; Song, W.; Shi, J.; Huang, M.; Mitlin, D. Sulfur-Nitrogen Rich Carbon as Stable High Capacity Potassium Ion Battery Anode: Performance and Storage Mechanisms. *Energy Storage Mater.* **2020**, 27, 212–225.
- (7) Mahmood, A.; Li, S.; Ali, Z.; Tabassum, H.; Zhu, B.; Liang, Z.; Meng, W.; Aftab, W.; Guo, W.; Zhang, H.; Yousaf, M.; Gao, S.; Zou, R.; Zhao, Y. Ultrafast Sodium/Potassium-Ion Intercalation into Hierarchically Porous Thin Carbon Shells. *Adv. Mater.* **2019**, *31*, 1805430.
- (8) Liu, L.; Chen, Y.; Xie, Y.; Tao, P.; Li, Q.; Yan, C. Understanding of the Ultrastable K-Ion Storage of Carbonaceous Anode. *Adv. Funct. Mater.* **2018**, 28, 1801989.
- (9) Chen, M.; Wang, W.; Liang, X.; Gong, S.; Liu, J.; Wang, Q.; Guo, S.; Yang, H. Sulfur/Oxygen Codoped Porous Hard Carbon Microspheres for High-Performance Potassium-Ion Batteries. *Adv. Energy Mater.* **2018**, *8*, 1800171.
- (10) Shen, C.; Cheng, T.; Liu, C.; Huang, L.; Cao, M.; Song, G.; Wang, D.; Lu, B.; Wang, J.; Qin, C.; Huang, X.; Peng, P.; Li, X.; Wu, Y. Bismuthene from Sonoelectrochemistry as a Superior Anode for Potassium-Ion Batteries. *J. Mater. Chem. A* **2020**, *8*, 453–460.

- (11) Ruan, J.; Mo, F.; Long, Z.; Song, Y.; Fang, F.; Sun, D.; Zheng, S. Tailor-Made Gives the Best Fits: Superior Na/K-Ion Storage Performance in Exclusively Confined Red Phosphorus System. ACS Nano 2020, 14, 12222–12233.
- (12) Ding, J.; Zhang, H.; Zhou, H.; Feng, J.; Zheng, X.; Zhong, C.; Paek, E.; Hu, W.; Mitlin, D. Sulfur-Grafted Hollow Carbon Spheres for Potassium-Ion Battery Anodes. *Adv. Mater.* **2019**, *31*, 1900429.
- (13) Hosaka, T.; Kubota, K.; Hameed, A. S.; Komaba, S. Research Development on K-Ion Batteries. *Chem. Rev.* **2020**, *120*, 6358–6466.
- (14) Wang, J.; Fan, L.; Liu, Z.; Chen, S.; Zhang, Q.; Wang, L.; Yang, H.; Yu, X.; Lu, B. *In Situ* Alloying Strategy for Exceptional Potassium Ion Batteries. *ACS Nano* **2019**, *13*, 3703–3713.
- (15) Su, S.; Liu, Q.; Wang, J.; Fan, L.; Ma, R.; Chen, S.; Han, X.; Lu, B. Control of SEI Formation for Stable Potassium-Ion Battery Anodes by Bi-MOF-Derived Nanocomposites. *ACS Appl. Mater. Interfaces* **2019**, *11*, 22474–22480.
- (16) Liu, P.; Wang, Y.; Gu, Q.; Nanda, J.; Watt, J.; Mitlin, D. Dendrite-Free Potassium Metal Anodes in a Carbonate Electrolyte. *Adv. Mater.* **2020**, *32*, 1906735.
- (17) Li, Z.; Shin, W.; Chen, Y.; Neuefeind, J. C.; Greaney, P. A.; Ji, X. Low Temperature Pyrolyzed Soft Carbon as High Capacity K-Ion Anode. *ACS Appl. Energy Mater.* **2019**, *2*, 4053–4058.
- (18) Kubota, K.; Dahbi, M.; Hosaka, T.; Kumakura, S.; Komaba, S. Towards K-Ion and Na-Ion Batteries as "Beyond Li-Ion. *Chem. Rev.* **2018**, *18*, 459–479.
- (19) Lian, P.; Dong, Y.; Wu, Z.-S.; Zheng, S.; Wang, X.; Sen, W.; Sun, C.; Qin, J.; Shi, X.; Bao, X. Alkalized Ti₃C₂ MXene Nanoribbons with Expanded Interlayer Spacing for High-Capacity Sodium and Potassium Ion Batteries. *Nano Energy* **2017**, *40*, 1–8.
- (20) Wu, X.; Zhao, W.; Wang, H.; Qi, X.; Xing, Z.; Zhuang, Q.; Ju, Z. Enhanced Capacity of Chemically Bonded Phosphorus/Carbon Composite as an Anode Material for Potassium-Ion Batteries. *J. Power Sources* **2018**, *378*, 460–467.
- (21) Jin, T.; Li, H.; Li, Y.; Jiao, L.; Chen, J. Intercalation Pseudocapacitance in Flexible and Self-Standing V_2O_3 Porous Nanofibers for High-Rate and Ultra-Stable K Ion Storage. *Nano Energy* **2018**, *50*, 462–467.
- (22) Cao, K.; Liu, H.; Li, W.; Xu, C.; Han, Q.; Zhang, Z.; Jiao, L. K₂Ti₆O₁₃ Nanorods for Potassium-Ion Battery Anodes. *J. Electroanal. Chem.* **2019**, 841, 51–55.
- (23) Wu, Y.; Huang, H. B.; Feng, Y.; Wu, Z. S.; Yu, Y. The Promise and Challenge of Phosphorus-Based Composites as Anode Materials for Potassium-Ion Batteries. *Adv. Mater.* **2019**, *31*, 1901414.
- (24) Zhang, Q.; Mao, J.; Pang, W. K.; Zheng, T.; Sencadas, V.; Chen, Y.; Liu, Y.; Guo, Z. Boosting the Potassium Storage Performance of Alloy-Based Anode Materials *via* Electrolyte Salt Chemistry. *Adv. Energy Mater.* **2018**, *8*, 1703288.
- (25) Xing, Z.; Qi, Y.; Jian, Z.; Ji, X. Polynanocrystalline Graphite: A New Carbon Anode with Superior Cycling Performance for K-Ion Batteries. ACS Appl. Mater. Interfaces 2017, 9, 4343–4351.
- (26) Xing, Z.; Jian, Z.; Luo, W.; Qi, Y.; Bommier, C.; Chong, E. S.; Li, Z.; Hu, L.; Ji, X. A Perylene Anhydride Crystal as a Reversible Electrode for K-Ion Batteries. *Energy Storage Mater.* **2016**, *2*, 63–68.
- (27) Qian, Y.; Jiang, S.; Li, Y.; Yi, Z.; Zhou, J.; Tian, J.; Lin, N.; Qian, Y. Water-Induced Growth of a Highly Oriented Mesoporous Graphitic Carbon Nanospring for Fast Potassium-Ion Adsorption/Intercalation Storage. *Angew. Chem., Int. Ed.* **2019**, *58*, 18108–18115.
- (28) Qin, L.; Xiao, N.; Zheng, J.; Lei, Y.; Zhai, D.; Wu, Y. Localized High-Concentration Electrolytes Boost Potassium Storage in High-Loading Graphite. *Adv. Energy Mater.* **2019**, *9*, 1902618.
- (29) Li, D.; Zhang, Y.; Sun, Q.; Zhang, S.; Wang, Z.; Liang, Z.; Si, P.; Ci, L. Hierarchically Porous Carbon Supported Sn₄P₃ as a Superior Anode Material for Potassium-Ion Batteries. *Energy Storage Mater.* **2019**, 23, 367–374.
- (30) Adekoya, D.; Li, M.; Hankel, M.; Lai, C.; Balogun, M.-S.; Tong, Y.; Zhang, S. Design of a 1D/2D C₃N₄/rGO Composite as an Anode Material for Stable and Effective Potassium Storage. *Energy Storage Mater.* **2020**, *25*, 495–501.

- (31) Zhang, R.; Huang, J.; Deng, W.; Bao, J.; Pan, Y.; Huang, S.; Sun, C. F. Safe, Low-Cost, Fast-Kinetics and Low-Strain Inorganic-Open-Framework Anode for Potassium-Ion Batteries. *Angew. Chem., Int. Ed.* **2019**, *58*, 16474–16479.
- (32) Zhang, C.; Qiao, Y.; Xiong, P.; Ma, W.; Bai, P.; Wang, X.; Li, Q.; Zhao, J.; Xu, Y.; Chen, Y.; Zeng, J. H.; Wang, F.; Xu, Y.; Jiang, J. X. Conjugated Microporous Polymers with Tunable Electronic Structure for High-Performance Potassium-Ion Batteries. *ACS Nano* **2019**, *13*, 745–754.
- (33) Liu, Z.; Wang, J.; Jia, X.; Li, W.; Zhang, Q.; Fan, L.; Ding, H.; Yang, H.; Yu, X.; Li, X.; Lu, B. Graphene Armored with a Crystal Carbon Shell for Ultrahigh-Performance Potassium Ion Batteries and Aluminum Batteries. ACS Nano 2019, 13, 10631–10642.
- (34) Chen, J.; Yang, B.; Hou, H.; Li, H.; Liu, L.; Zhang, L.; Yan, X. Disordered, Large Interlayer Spacing, and Oxygen-Rich Carbon Nanosheets for Potassium Ion Hybrid Capacitor. *Adv. Energy Mater.* **2019**, *9*, 1803894.
- (35) Share, K.; Cohn, A. P.; Carter, R.; Rogers, B.; Pint, C. L. Role of Nitrogen-Doped Graphene for Improved High-Capacity Potassium Ion Battery Anodes. *ACS Nano* **2016**, *10*, 9738–9744.
- (36) Zhang, H.; Luo, C.; He, H.; Wu, H. H.; Zhang, L.; Zhang, Q.; Wang, H.; Wang, M. S. Nano-Size Porous Carbon Spheres as a High-Capacity Anode with High Initial Coulombic Efficiency for Potassium-Ion Batteries. *Nanoscale Horiz.* **2020**, *5*, 895–903.
- (37) Ge, J.; Wang, B.; Zhou, J.; Liang, S.; Rao, A. M.; Lu, B. Hierarchically Structured Nitrogen-Doped Carbon Microspheres for Advanced Potassium Ion Batteries. ACS Mater. Lett. 2020, 2, 853–860
- (38) Luo, W.; Wan, J.; Ozdemir, B.; Bao, W.; Chen, Y.; Dai, J.; Lin, H.; Xu, Y.; Gu, F.; Barone, V.; Hu, L. Potassium Ion Batteries with Graphitic Materials. *Nano Lett.* **2015**, *15*, 7671–7677.
- (39) Fan, L.; Ma, R.; Zhang, Q.; Jia, X.; Lu, B. Graphite Anode for a Potassium-Ion Battery with Unprecedented Performance. *Angew. Chem., Int. Ed.* **2019**, *58*, 10500–10505.
- (40) Jian, Z.; Luo, W.; Ji, X. Carbon Electrodes for K-Ion Batteries. *J. Am. Chem. Soc.* **2015**, *137*, 11566–11569.
- (41) Hong, W.; Zhang, Y.; Yang, L.; Tian, Y.; Ge, P.; Hu, J.; Wei, W.; Zou, G.; Hou, H.; Ji, X. Carbon Quantum Dot Micelles Tailored Hollow Carbon Anode for Fast Potassium and Sodium Storage. *Nano Energy* **2019**, *65*, 104038.
- (42) Cohn, A. P.; Muralidharan, N.; Carter, R.; Share, K.; Oakes, L.; Pint, C. L. Durable Potassium Ion Battery Electrodes from High-Rate Cointercalation into Graphitic Carbons. *J. Mater. Chem. A* **2016**, *4*, 14954–14959.
- (43) Xu, Z.; Lv, X.; Chen, J.; Jiang, L.; Lai, Y.; Li, J. Dispersion-Corrected DFT Investigation on Defect Chemistry and Potassium Migration in Potassium-Graphite Intercalation Compounds for Potassium Ion Batteries Anode Materials. *Carbon* **2016**, *107*, 885–
- (44) Zhao, J.; Zou, X.; Zhu, Y.; Xu, Y.; Wang, C. Electrochemical Intercalation of Potassium into Graphite. *Adv. Funct. Mater.* **2016**, 26, 8103–8110.
- (45) Wang, L.; Yang, J.; Li, J.; Chen, T.; Chen, S.; Wu, Z.; Qiu, J.; Wang, B.; Gao, P.; Niu, X.; Li, H. Graphite as a Potassium Ion Battery Anode in Carbonate-Based Electrolyte and Ether-Based Electrolyte. *J. Power Sources* **2019**, *409*, 24–30.
- (46) Komaba, S.; Hasegawa, T.; Dahbi, M.; Kubota, K. Potassium Intercalation into Graphite to Realize High-Voltage/High-Power Potassium-Ion Batteries and Potassium-Ion Capacitors. *Electrochem. Commun.* **2015**, *60*, 172–175.
- (47) An, Y.; Fei, H.; Zeng, G.; Ci, L.; Xi, B.; Xiong, S.; Feng, J. Commercial Expanded Graphite as a Low–Cost, Long-Cycling Life Anode for Potassium–Ion Batteries with Conventional Carbonate Electrolyte. *J. Power Sources* **2018**, 378, 66–72.
- (48) Zhang, W.; Yin, J.; Sun, M.; Wang, W.; Chen, C.; Altunkaya, M.; Emwas, A. H.; Han, Y.; Schwingenschlögl, U.; Alshareef, H. N. Direct Pyrolysis of Supermolecules: An Ultrahigh Edge-Nitrogen Doping Strategy of Carbon Anodes for Potassium-Ion Batteries. *Adv. Mater.* **2020**, *32*, 2000732.

- (49) Zhang, W.; Cao, Z.; Wang, W.; Alhajji, E.; Emwas, A. H.; Costa, P.; Cavallo, L.; Alshareef, H. N. A Site-Selective Doping Strategy of Carbon Anodes with Remarkable K-Ion Storage Capacity. *Angew. Chem., Int. Ed.* **2020**, *59*, 4448–4455.
- (50) Bin, D. S.; Lin, X. J.; Sun, Y. G.; Xu, Y. S.; Zhang, K.; Cao, A. M.; Wan, L. J. Engineering Hollow Carbon Architecture for High-Performance K-Ion Battery Anode. *J. Am. Chem. Soc.* **2018**, *140*, 7127–7134.
- (51) Cao, B.; Zhang, Q.; Liu, H.; Xu, B.; Zhang, S.; Zhou, T.; Mao, J.; Pang, W. K.; Guo, Z.; Li, A.; Zhou, J.; Chen, X.; Song, H. Graphitic Carbon Nanocage as a Stable and High Power Anode for Potassium-Ion Batteries. *Adv. Energy Mater.* **2018**, *8*, 1801149.
- (52) Zhang, W.; Ming, J.; Zhao, W.; Dong, X.; Hedhili, M. N.; Costa, P. M. F. J.; Alshareef, H. N. Graphitic Nanocarbon with Engineered Defects for High-Performance Potassium-Ion Battery Anodes. *Adv. Funct. Mater.* **2019**, *29*, 1903641.
- (53) Adams, R. A.; Syu, J. M.; Zhao, Y.; Lo, C. T.; Varma, A.; Pol, V. G. Binder-Free N- and O-Rich Carbon Nanofiber Anodes for Long Cycle Life K-Ion Batteries. *ACS Appl. Mater. Interfaces* **2017**, *9*, 17872–17881.
- (54) Hu, X.; Liu, Y.; Chen, J.; Yi, L.; Zhan, H.; Wen, Z. Fast Redox Kinetics in Bi-Heteroatom Doped 3D Porous Carbon Nanosheets for High-Performance Hybrid Potassium-Ion Battery Capacitors. *Adv. Energy Mater.* **2019**, *9*, 1901533.
- (55) Xu, D.; Chen, C.; Xie, J.; Zhang, B.; Miao, L.; Cai, J.; Huang, Y.; Zhang, L. A Hierarchical N/S-Codoped Carbon Anode Fabricated Facilely from Cellulose/Polyaniline Microspheres for High-Performance Sodium-Ion Batteries. *Adv. Energy Mater.* **2016**, *6*, 1501929.
- (56) Qie, L.; Chen, W.; Xiong, X.; Hu, C.; Zou, F.; Hu, P.; Huang, Y. Sulfur-Doped Carbon with Enlarged Interlayer Distance as a High-Performance Anode Material for Sodium-Ion Batteries. *Adv. Sci.* **2015**, 2, 1500195.
- (57) Yang, W.; Zhou, J.; Wang, S.; Zhang, W.; Wang, Z.; Lv, F.; Wang, K.; Sun, Q.; Guo, S. Freestanding Film Made by Necklace-Like N-Doped Hollow Carbon with Hierarchical Pores for High-Performance Potassium-Ion Storage. *Energy Environ. Sci.* **2019**, *12*, 1605–1612.
- (58) Ruan, J.; Zhao, Y.; Luo, S.; Yuan, T.; Yang, J.; Sun, D.; Zheng, S. Fast and Stable Potassium-Ion Storage Achieved by *in Situ* Molecular Self-Assembling N/O Dual-Doped Carbon Network. *Energy Storage Mater.* **2019**, *23*, 46–54.
- (59) Li, J.; Qin, W.; Xie, J.; Lei, H.; Zhu, Y.; Huang, W.; Xu, X.; Zhao, Z.; Mai, W. Sulphur-Doped Reduced Graphene Oxide Sponges as High-Performance Free-Standing Anodes for K-Ion Storage. *Nano Energy* **2018**, *53*, 415–424.
- (60) Xie, X.; Qi, S.; Wu, D.; Wang, H.; Li, F.; Peng, X.; Cai, J.; Liang, J.; Ma, J. Porous Surfur-Doped Hard Carbon for Excellent Potassium Storage. *Chin. Chem. Lett.* **2020**, *31*, 223–226.
- (61) Shi, X.; Chen, Y.; Lai, Y.; Zhang, K.; Li, J.; Zhang, Z. Metal Organic Frameworks Templated Sulfur-Doped Mesoporous Carbons as Anode Materials for Advanced Sodium Ion Batteries. *Carbon* **2017**, 123, 250–258.
- (62) Li, Y.; Zhong, W.; Yang, C.; Zheng, F.; Pan, Q.; Liu, Y.; Wang, G.; Xiong, X.; Liu, M. N/S Codoped Carbon Microboxes with Expanded Interlayer Distance toward Excellent Potassium Storage. *Chem. Eng. J.* **2019**, 358, 1147–1154.
- (63) Wang, H.; Gao, Q.; Hu, J. High Hydrogen Storage Capacity of Porous Carbons Prepared by Using Activated Carbon. *J. Am. Chem. Soc.* **2009**, *131*, 7016–7022.
- (64) Qu, D. Investigation of Hydrogen Physisorption Active Sites on the Surface of Porous Carbonaceous Materials. *Chem. Eur. J.* **2008**, *14*, 1040–1046.
- (65) Xu, W.; Lv, C.; Zou, Y.; Ren, J.; She, X.; Zhu, Y.; Zhang, Y.; Chen, S.; Yang, X.; Zhan, T.; Sun, J.; Yang, D. Mechanistic Insight into High-Efficiency Sodium Storage Based on N/O/P-Functionalized Ultrathin Carbon Nanosheet. *J. Power Sources* **2019**, 442, 227184.

- (66) Cuesta, A.; Dhamelincourt, P.; Laureyns, J.; Martinez-alonso, A.; Tascon, J. M. D. Raman Microprobe Studies on Carbon Materials. *Carbon* **1994**, 32, 1523–1532.
- (67) Wang, H.; Liu, S.; Huang, Y. Preparation and Characterization of SnO₂ and Carbon Co-Coated LiFePO₄ Cathode Materials. *J. Nanosci. Nanotechnol.* **2014**, *14*, 3281–3283.
- (68) Ni, D.; Sun, W.; Wang, Z.; Bai, Y.; Lei, H.; Lai, X.; Sun, K. Heteroatom-Doped Mesoporous Hollow Carbon Spheres for Fast Sodium Storage with an Ultralong Cycle Life. *Adv. Energy Mater.* **2019**, *9*, 1900036.
- (69) Niu, J.; Shao, R.; Liang, J.; Dou, M.; Li, Z.; Huang, Y.; Wang, F. Biomass-Derived Mesopore-Dominant Porous Carbons with Large Specific Surface Area and High Defect Density as High Performance Electrode Materials for Li-Ion Batteries and Supercapacitors. *Nano Energy* **2017**, *36*, 322–330.
- (70) Bonhomme, F.; Lassègues, J. C.; Servant, L. Raman Spectroelectrochemistry of a Carbon Supercapacitor. *J. Electrochem. Soc.* **2001**, *148*, E450.
- (71) Liu, H.; Liu, X.; Wang, H.; Zheng, Y.; Zhang, H.; Shi, J.; Liu, W.; Huang, M.; Kan, J.; Zhao, X.; Li, D. High-Performance Sodium-Ion Capacitor Constructed by Well-Matched Dual-Carbon Electrodes from a Single Biomass. ACS Sustainable Chem. Eng. 2019, 7, 12188—12199
- (72) Qiu, S.; Xiao, L.; Sushko, M. L.; Han, K. S.; Shao, Y.; Yan, M.; Liang, X.; Mai, L.; Feng, J.; Cao, Y.; Ai, X.; Yang, H.; Liu, J. Manipulating Adsorption-Insertion Mechanisms in Nanostructured Carbon Materials for High-Efficiency Sodium Ion Storage. *Adv. Energy Mater.* **2017**, *7*, 1700403.
- (73) Yun, Y. S.; Le, V.-D.; Kim, H.; Chang, S.-J.; Baek, S. J.; Park, S.; Kim, B. H.; Kim, Y.-H.; Kang, K.; Jin, H.-J. Effects of Sulfur Doping on Graphene-Based Nanosheets for Use as Anode Materials in Lithium-Ion Batteries. *J. Power Sources* **2014**, *262*, 79–85.
- (74) Li, Z.; Dong, Y.; Feng, J.; Xu, T.; Ren, H.; Gao, C.; Li, Y.; Cheng, M.; Wu, W.; Wu, M. Controllably Enriched Oxygen Vacancies through Polymer Assistance in Titanium Pyrophosphate as a Super Anode for Na/K-Ion Batteries. *ACS Nano* **2019**, *13*, 9227–9236.
- (75) Wu, T.; Jing, M.; Yang, L.; Zou, G.; Hou, H.; Zhang, Y.; Cao, X.; Ji, X. Controllable Chain-Length for Covalent Sulfur-Carbon Materials Enabling Stable and High-Capacity Sodium Storage. *Adv. Energy Mater.* **2019**, *9*, 1803478.
- (76) Qian, J.; Wu, F.; Ye, Y.; Zhang, M.; Huang, Y.; Xing, Y.; Qu, W.; Li, L.; Chen, R. Boosting Fast Sodium Storage of a Large-Scalable Carbon Anode with an Ultralong Cycle Life. *Adv. Energy Mater.* **2018**, *8*, 1703159.
- (77) Jin, Q.; Li, W.; Wang, K.; Feng, P.; Li, H.; Gu, T.; Zhou, M.; Wang, W.; Cheng, S.; Jiang, K. Experimental Design and Theoretical Calculation for Sulfur-Doped Carbon Nanofibers as a High Performance Sodium-Ion Battery Anode. *J. Mater. Chem. A* **2019**, 7, 10239–10245.
- (78) Liu, S.; Cai, Y.; Zhao, X.; Liang, Y.; Zheng, M.; Hu, H.; Dong, H.; Jiang, S.; Liu, Y.; Xiao, Y. Sulfur-Doped Nanoporous Carbon Spheres with Ultrahigh Specific Surface Area and High Electrochemical Activity for Supercapacitor. *J. Power Sources* **2017**, 360, 373–382.
- (79) Tian, S.; Guan, D.; Lu, J.; Zhang, Y.; Liu, T.; Zhao, X.; Yang, C.; Nan, J. Synthesis of the Electrochemically Stable Sulfur-Doped Bamboo Charcoal as the Anode Material of Potassium-Ion Batteries. *J. Power Sources* **2020**, *448*, 227572.
- (80) Qiang, Z.; Chen, Y.-M.; Xia, Y.; Liang, W.; Zhu, Y.; Vogt, B. D. Ultra-Long Cycle Life, Low-Cost Room Temperature Sodium-Sulfur Batteries Enabled by Highly Doped (N,S) Nanoporous Carbons. *Nano Energy* **2017**, *32*, 59–66.
- (81) Wang, X.; Li, G.; Hassan, F. M.; Li, J.; Fan, X.; Batmaz, R.; Xiao, X.; Chen, Z. Sulfur Covalently Bonded Graphene with Large Capacity and High Rate for High-Performance Sodium-Ion Batteries Anodes. *Nano Energy* **2015**, *15*, 746–754.
- (82) Xia, L.; Wu, X.; Wang, Y.; Niu, Z.; Liu, Q.; Li, T.; Shi, X.; Asiri, A. M.; Sun, X. S-Doped Carbon Nanospheres: An Efficient

- Electrocatalyst toward Artificial N₂ Fixation to NH₃. Small Methods **2019**, 3, 1800251.
- (83) Yan, J.; Li, W.; Feng, P.; Wang, R.; Jiang, M.; Han, J.; Cao, S.; Wang, K.; Jiang, K. Enhanced Na⁺ Pseudocapacitance in a P, S Co-Doped Carbon Anode Arising from the Surface Modification by Sulfur and Phosphorus with C–S–P Coupling. *J. Mater. Chem. A* **2020**, *8*, 422–432.
- (84) Zou, G.; Wang, C.; Hou, H.; Wang, C.; Qiu, X.; Ji, X. Controllable Interlayer Spacing of Sulfur-Doped Graphitic Carbon Nanosheets for Fast Sodium-Ion Batteries. *Small* **2017**, *13*, 1700762.
- (85) Stephenson, T.; Hazelton, M.; Kupsta, M.; Lepore, J.; Andreassen, E. J.; Hoff, A.; Newman, B.; Eaton, P.; Gray, M.; Mitlin, D. Thiophene Mitigates High Temperature Fouling of Metal Surfaces in Oil Refining. *Fuel* **2015**, *139*, 411–424.
- (86) Bommier, C.; Mitlin, D.; Ji, X. Internal Structure Na Storage Mechanisms Electrochemical Performance Relations in Carbons. *Prog. Mater. Sci.* **2018**, *97*, 170–203.
- (87) Fan, L.; Ma, R.; Yang, Y.; Chen, S.; Lu, B. Covalent Sulfur for Advanced Room Temperature Sodium-Sulfur Batteries. *Nano Energy* **2016**, 28, 304–310.
- (88) Liu, P.; Mitlin, D. Emerging Potassium Metal Anodes: Perspectives on Control of the Electrochemical Interfaces. *Acc. Chem. Res.* **2020**, *53*, 1161–1175.
- (89) Chen, S.; Feng, Y.; Wang, J.; Zhang, E.; Yu, X.; Lu, B. Free-Standing N-Doped Hollow Carbon Fibers as High-Performance Anode for Potassium Ion Batteries. *Sci. China Mater.* **2020**, DOI: 10.1007/s40843-020-1465-8.
- (90) Lu, C.; Sun, Z.; Yu, L.; Lian, X.; Yi, Y.; Li, J.; Liu, Z.; Dou, S.; Sun, J. Enhanced Kinetics Harvested in Heteroatom Dual-Doped Graphitic Hollow Architectures toward High Rate Printable Potassium-Ion Batteries. *Adv. Energy Mater.* **2020**, *10*, 2001161.
- (91) Shao, M.; Li, C.; Li, T.; Zhao, H.; Yu, W.; Wang, R.; Zhang, J.; Yin, L. Pushing the Energy Output and Cycling Lifespan of Potassium-Ion Capacitor to High Level through Metal—Organic Framework Derived Porous Carbon Microsheets Anode. *Adv. Funct. Mater.* **2020**, *30*, 2006561.
- (92) Xia, G.; Wang, C.; Jiang, P.; Lu, J.; Diao, J.; Chen, Q. Nitrogen/Oxygen Co-Doped Mesoporous Carbon Octahedrons for High-Performance Potassium-Ion Batteries. *J. Mater. Chem. A* **2019**, *7*, 12317—12324
- (93) Yang, B.; Chen, J.; Liu, L.; Ma, P.; Liu, B.; Lang, J.; Tang, Y.; Yan, X. 3D Nitrogen-Doped Framework Carbon for High-Performance Potassium Ion Hybrid Capacitor. *Energy Storage Mater.* **2019**, 23, 522–529
- (94) Li, H.; Cheng, Z.; Zhang, Q.; Natan, A.; Yang, Y.; Cao, D.; Zhu, H. Bacterial-Derived, Compressible, and Hierarchical Porous Carbon for High-Performance Potassium-Ion Batteries. *Nano Lett.* **2018**, *18*, 7407–7413.
- (95) Zhao, X.; Tang, Y.; Ni, C.; Wang, J.; Star, A.; Xu, Y. Free-Standing Nitrogen-Doped Cup-Stacked Carbon Nanotube Mats for Potassium-Ion Battery Anodes. ACS Appl. Energy Mater. 2018, 1, 1703–1707.
- (96) Wang, Y.; Wang, Z.; Chen, Y.; Zhang, H.; Yousaf, M.; Wu, H.; Zou, M.; Cao, A.; Han, R. P. S. Hyperporous Sponge Interconnected by Hierarchical Carbon Nanotubes as a High-Performance Potassium-Ion Battery Anode. *Adv. Mater.* **2018**, *30*, 1802074.
- (97) Xie, Y.; Chen, Y.; Liu, L.; Tao, P.; Fan, M.; Xu, N.; Shen, X.; Yan, C. Ultra-High Pyridinic N-Doped Porous Carbon Monolith Enabling High-Capacity K-Ion Battery Anodes for Both Half-Cell and Full-Cell Applications. *Adv. Mater.* **2017**, *29*, 1702268.
- (98) Zhou, X.; Chen, L.; Zhang, W.; Wang, J.; Liu, Z.; Zeng, S.; Xu, R.; Wu, Y.; Ye, S.; Feng, Y.; Cheng, X.; Peng, Z.; Li, X.; Yu, Y. Three-Dimensional Ordered Macroporous Metal-Organic Framework Single Crystal-Derived Nitrogen-Doped Hierarchical Porous Carbon for High-Performance Potassium-Ion Batteries. *Nano Lett.* **2019**, *19*, 4965–4973.
- (99) Liu, Y.; Yang, C.; Pan, Q.; Li, Y.; Wang, G.; Ou, X.; Zheng, F.; Xiong, X.; Liu, M.; Zhang, Q. Nitrogen-Doped Bamboo-Like Carbon

- Nanotubes as Anode Material for High Performance Potassium Ion Batteries. J. Mater. Chem. A 2018, 6, 15162–15169.
- (100) Lu, G.; Wang, H.; Zheng, Y.; Zhang, H.; Yang, Y.; Shi, J.; Huang, M.; Liu, W. Metal-Organic Framework Derived N-Doped CNT@ Porous Carbon for High-Performance Sodium- and Potassium-Ion Storage. *Electrochim. Acta* 2019, 319, 541–551.
- (101) Wang, H.; Mitlin, D.; Ding, J.; Li, Z.; Cui, K. Excellent Energy—Power Characteristics from a Hybrid Sodium Ion Capacitor Based on Identical Carbon Nanosheets in Both Electrodes. *J. Mater. Chem. A* **2016**, *4*, 5149—5158.
- (102) Wang, W.; Zhou, J.; Wang, Z.; Zhao, L.; Li, P.; Yang, Y.; Yang, C.; Huang, H.; Guo, S. Short-Range Order in Mesoporous Carbon Boosts Potassium-Ion Battery Performance. *Adv. Energy Mater.* **2018**, *8*, 1701648.
- (103) Tai, Z.; Liu, Y.; Zhang, Q.; Zhou, T.; Guo, Z.; Liu, H. K.; Dou, S. X. Ultra-Light and Flexible Pencil-Trace Anode for High Performance Potassium-Ion and Lithium-Ion Batteries. *Green Energy Environ.* **2017**, *2*, 278–284.
- (104) Yang, Y.; Li, D.; Zhang, J.; Suo, G.; Yu, Q.; Feng, L.; Hou, X.; Ye, X.; Zhang, L.; Wang, W. Sn Nanoparticles Anchored on N Doped Porous Carbon as an Anode for Potassium Ion Batteries. *Mater. Lett.* **2019**, *256*, 126613.
- (105) Cui, Y.; Liu, W.; Wang, X.; Li, J.; Zhang, Y.; Du, Y.; Liu, S.; Wang, H.; Feng, W.; Chen, M. Bioinspired Mineralization under Freezing Conditions: An Approach to Fabricate Porous Carbons with Complicated Architecture and Superior K⁺ Storage Performance. *ACS Nano* **2019**, *13*, 11582–11592.
- (106) Xu, Y.; Zhang, C.; Zhou, M.; Fu, Q.; Zhao, C.; Wu, M.; Lei, Y. Highly Nitrogen Doped Carbon Nanofibers with Superior Rate Capability and Cyclability for Potassium Ion Batteries. *Nat. Commun.* **2018**, *9*, 1720.
- (107) Tong, Z.; Yang, R.; Wu, S.; Shen, D.; Jiao, T.; Zhang, K.; Zhang, W.; Lee, C. S. Surface-Engineered Black Niobium Oxide@ Graphene Nanosheets for High-Performance Sodium-/Potassium-Ion Full Batteries. *Small* **2019**, *15*, 1901272.
- (108) Li, Y.; Zhang, Q.; Yuan, Y.; Liu, H.; Yang, C.; Lin, Z.; Lu, J. Surface Amorphization of Vanadium Dioxide (B) for K-Ion Battery. *Adv. Energy Mater.* **2020**, *10*, 2000717.
- (109) Shi, Z.; Ru, Q.; Cheng, S.; Hou, X.; Chen, F.; Chi-Chung Ling, F. Hierarchically Rambutan-Like $\rm Zn_3V_3O_8$ Hollow Spheres as Anodes for Lithium-/Potassium-Ion Batteries. *Energy Technol.* **2020**, *8*, 2000010.
- (110) Lee, B.; Kim, M.; Kim, S.; Nanda, J.; Kwon, S. J.; Jang, H. D.; Mitlin, D.; Lee, S. W. High Capacity Adsorption—Dominated Potassium and Sodium Ion Storage in Activated Crumpled Graphene. *Adv. Energy Mater.* **2020**, *10*, 1903280.
- (111) Yu, F.; Liu, Z.; Zhou, R.; Tan, D.; Wang, H.; Wang, F. Pseudocapacitance Contribution in Boron-Doped Graphite Sheets for Anion Storage Enables High-Performance Sodium-Ion Capacitors. *Mater. Horiz.* **2018**, *5*, 529–535.
- (112) Sun, D.; Wang, L.; Li, Y.; Yang, Y.; Zhou, X.; Ma, G.; Lei, Z. Confined Metal Sulfides Nanoparticles into Porous Carbon Nanosheets with Surface-Controlled Reactions for Fast and Stable Lithium-Ion Batteries. *ChemElectroChem* **2019**, *6*, 4464–4470.
- (113) Feng, W.; Cui, Y.; Liu, W.; Wang, H.; Zhang, Y.; Du, Y.; Liu, S.; Wang, H.; Gao, X.; Wang, T. Rigid-Flexible Coupling Carbon Skeleton and Potassium-Carbonate-Dominated Solid Electrolyte Interface Achieving Superior Potassium-Ion Storage. *ACS Nano* **2020**, *14*, 4938–4949.
- (114) Wang, G.; Li, F.; Liu, D.; Zheng, D.; Abeggien, C. J.; Luo, Y.; Yang, X.-Q.; Ding, T.; Qu, D. High Performance Lithium-Ion and Lithium-Sulfur Batteries Using Prelithiated Phosphorus/Carbon Composite Anode. *Energy Storage Mater.* **2020**, *24*, 147–152.
- (115) Hu, X.; Zhong, G.; Li, J.; Liu, Y.; Yuan, J.; Chen, J.; Zhan, H.; Wen, Z. Hierarchical Porous Carbon Nanofibers for Compatible Anode and Cathode of Potassium-Ion Hybrid Capacitor. *Energy Environ. Sci.* **2020**, *13*, 2431–2440.